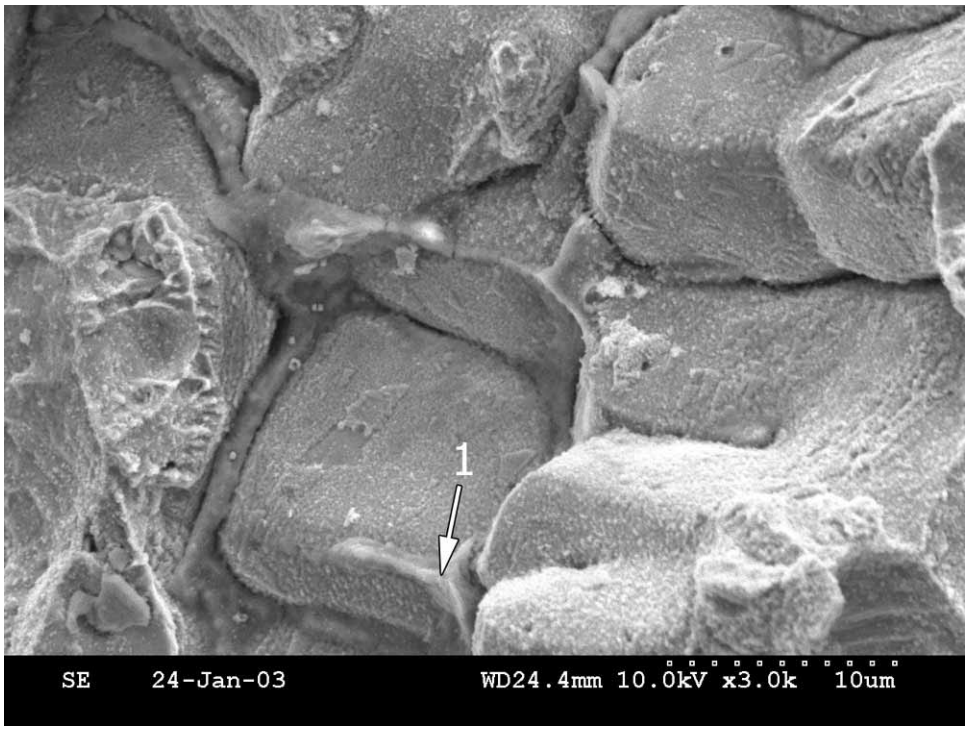

SE 3,000X

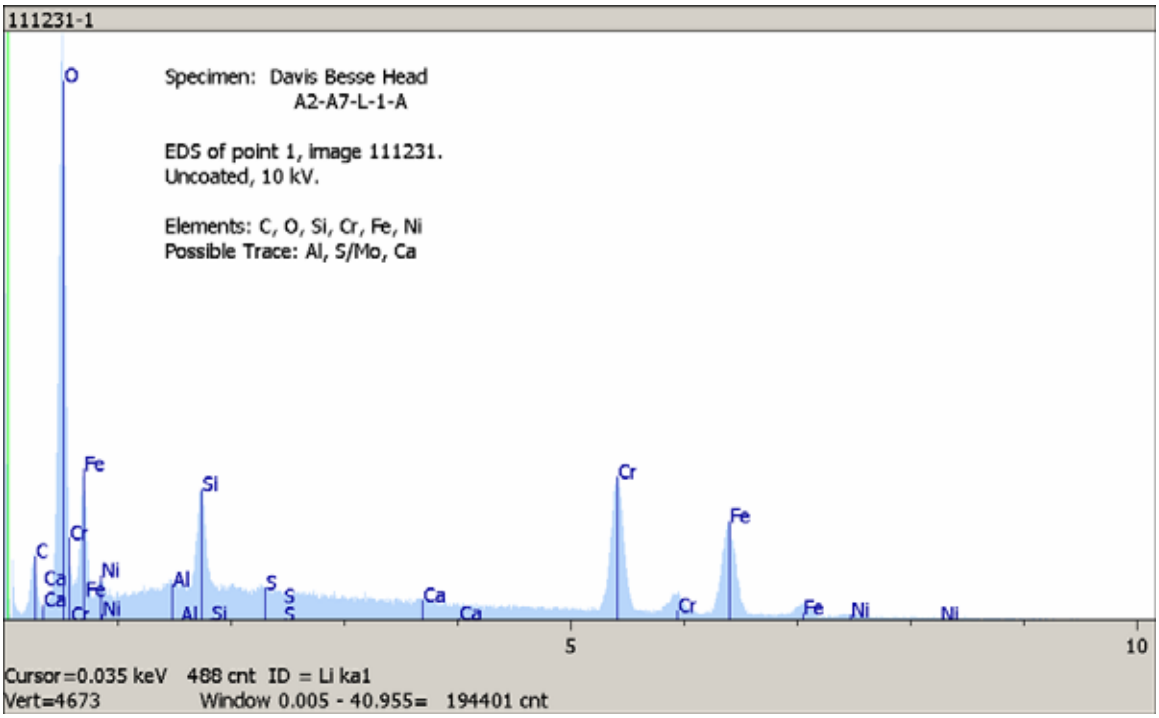

EDS results for point 1 above.

Figure 6.4.1.8: Higher magnification SE micrograph and EDS results for a grain boundary deposit near area "E". This area contained primarily carbon, oxygen, silicon, chromium, iron, and nickel. Lesser amounts of aluminum, sulfur, and calcium were also detected.

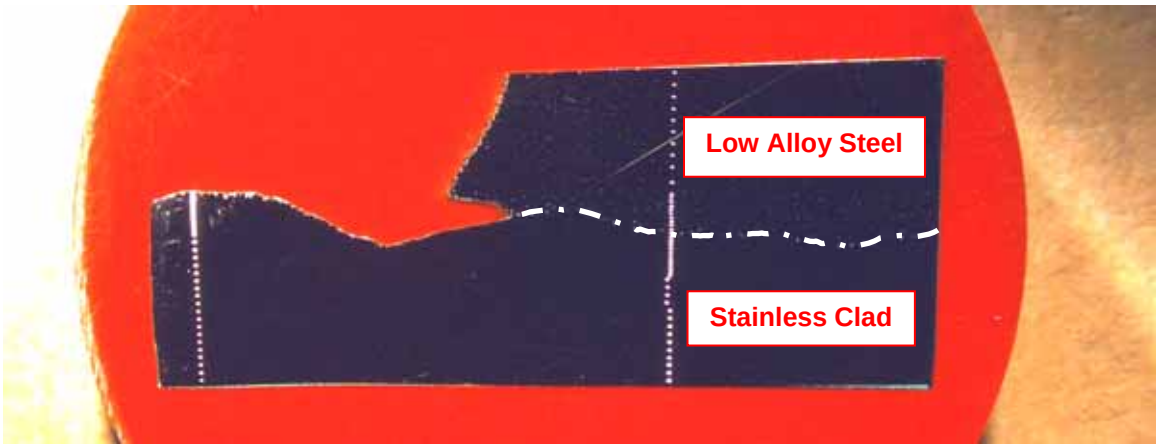

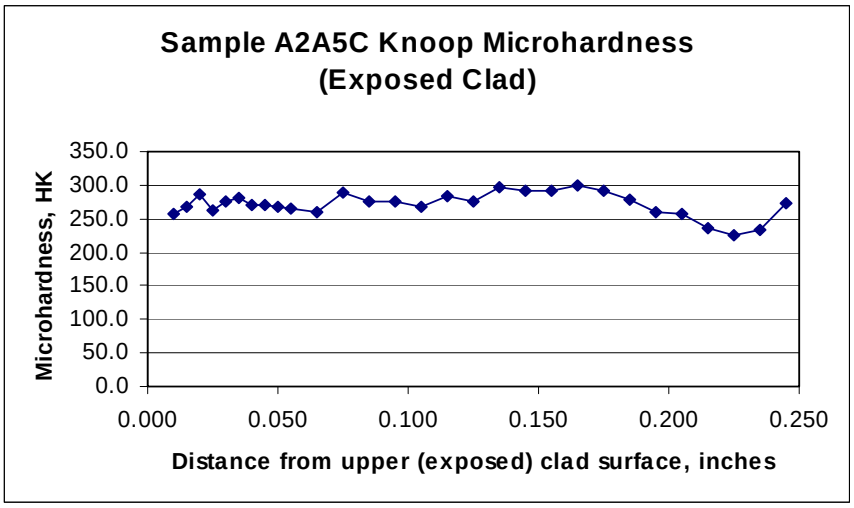

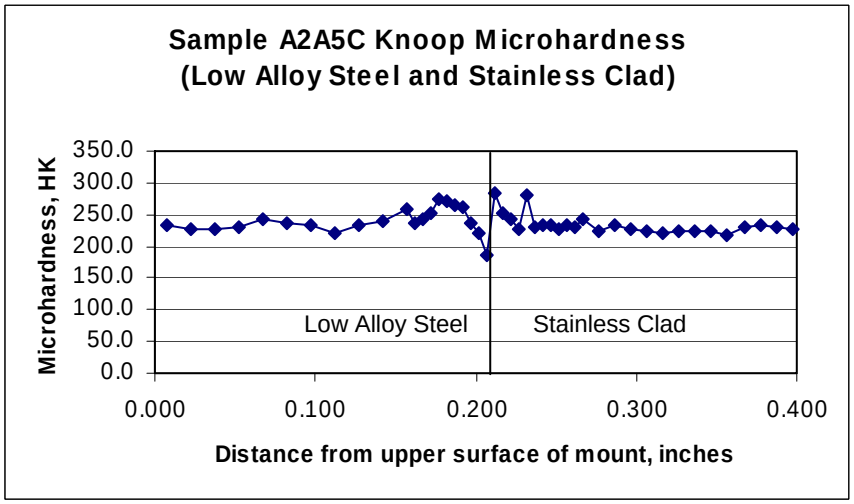

Figure 6.5.1.1: 4X macro photograph of metallographic mount A2A5C, along with Knoop microhardness data. Refer to Figure 5.13 for the sample orientation. The two Knoop microhardness traverse lines are visible in the macro photo. The significant microhardness variations occur in the heat affected zone of the low alloy steel and the cladding adjacent to the fusion line.

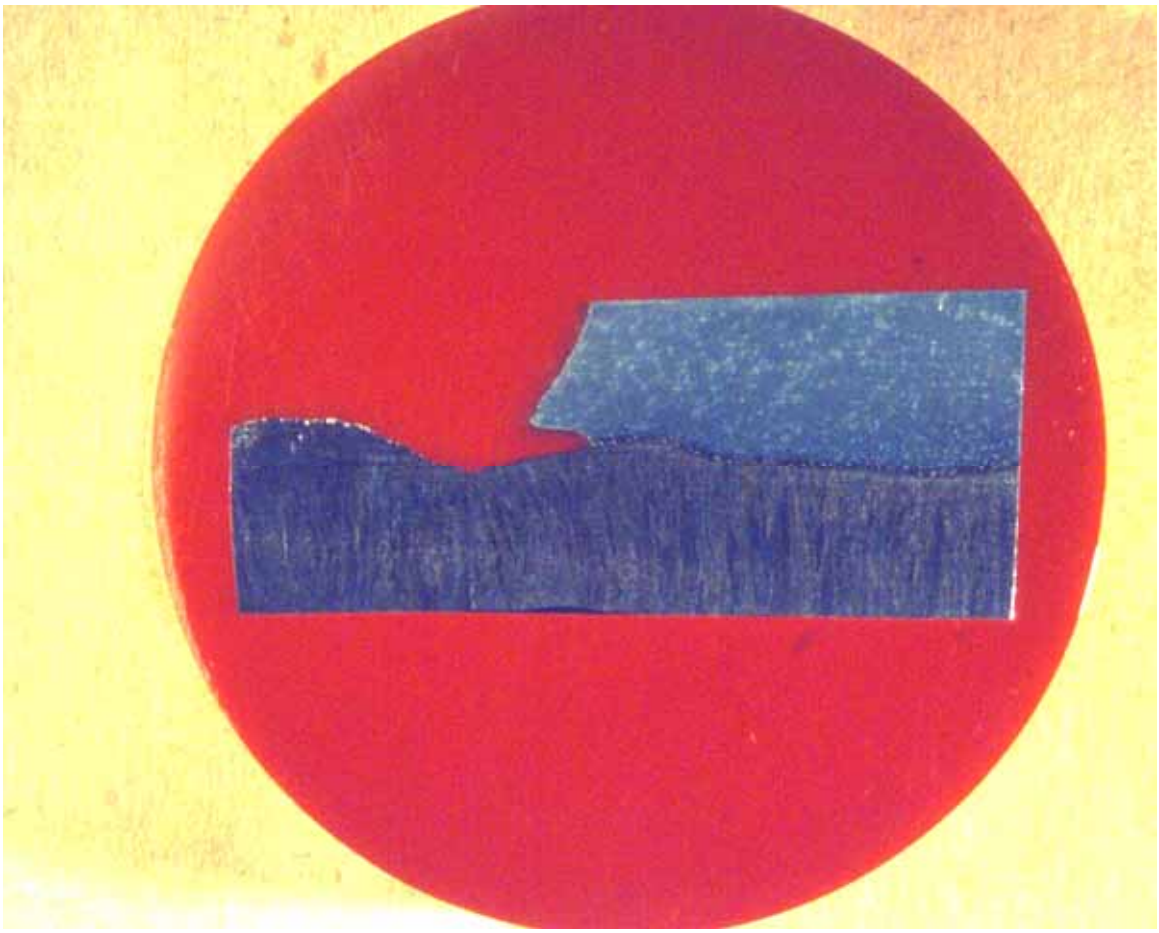

4X

Figure 6.5.1.2: Low magnification photograph of mounted sample A2A5C after chemical etching to reveal the cladding microstructure. It did not appear that a weld deposition change occurred in this region.

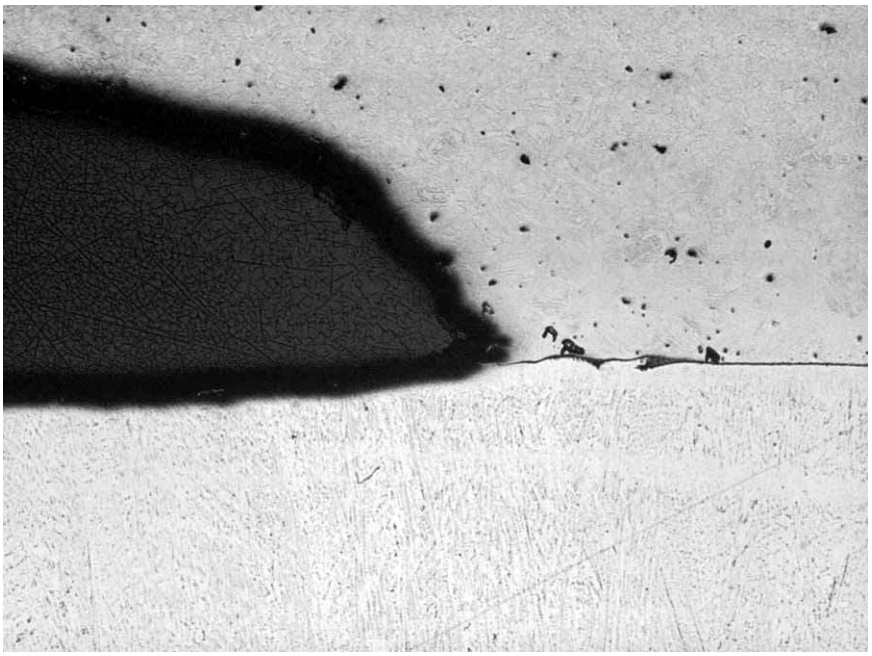

Etched 48X

Figure 6.5.1.3: Micrograph showing the undercutting due to boric acid corrosion in the RV head low alloy steel at the interface between low alloy steel (above the notch) and stainless steel cladding (below the notch).

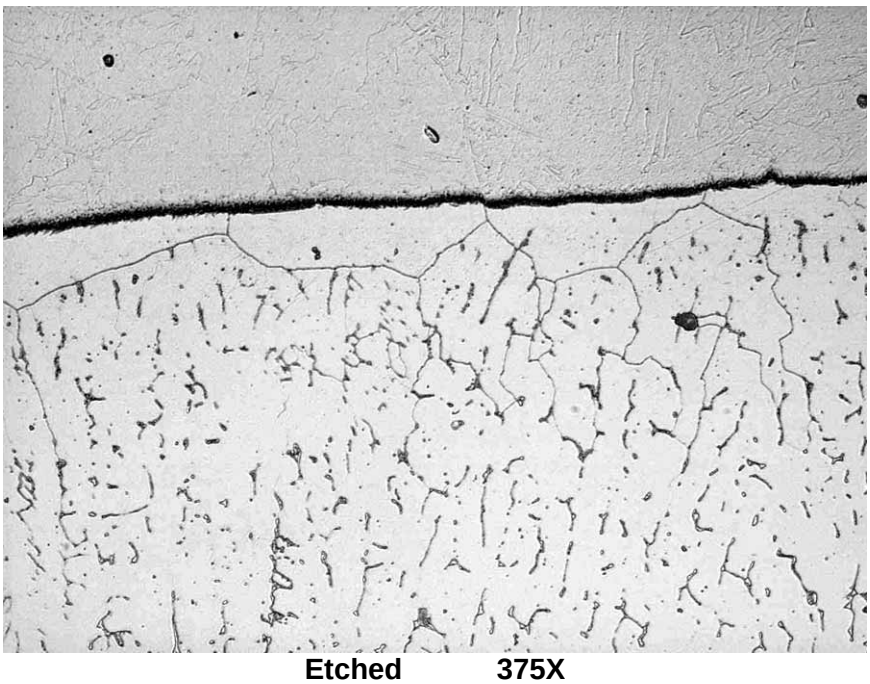

Etched 375X

Figure 6.5.1.4: Micrograph showing the interface between low alloy steel (above) and stainless steel cladding (below). The austenitic grains in the first interface layer on the stainless steel cladding side are equiaxed and growing preferentially from the ferrite grains (low alloy steel). The subsequent grain growth in the cladding is columnar.

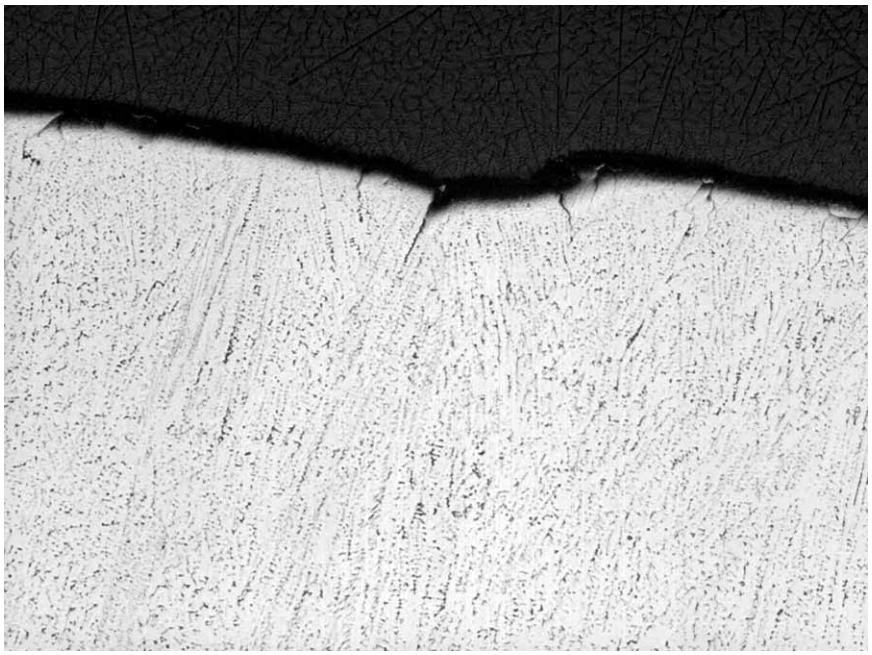

Etched 100X

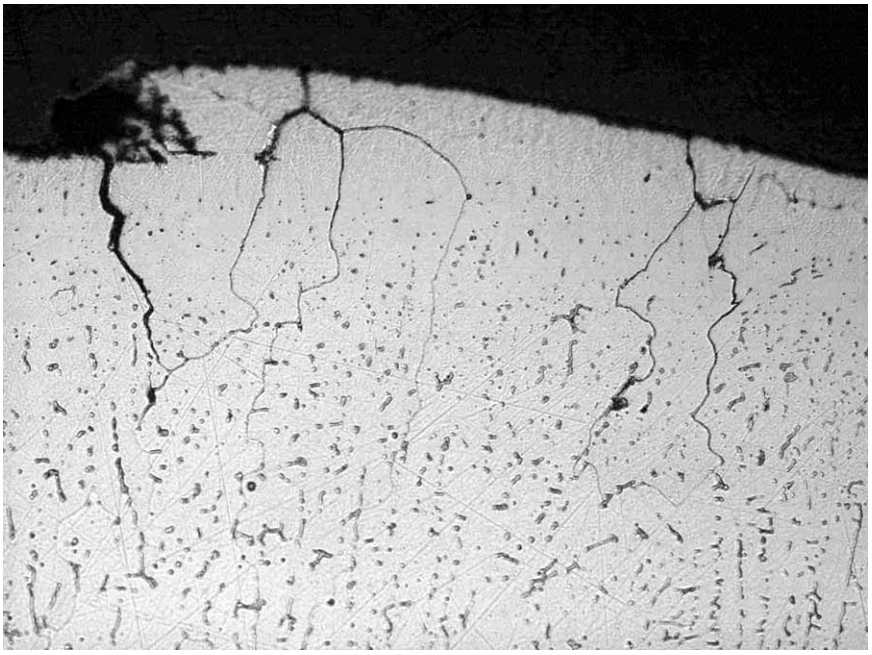

Etched 375X

Figure 6.5.1.5: Micrographs of the cladding surface exposed due to boric acid corrosion of the RV head low alloy steel. Intergranular attack (IGA) of stainless steel cladding to a depth of the first or second layers of grains is clearly visible. The IGA is probably due to oxygenated and highly concentrated boric acid. There was no evidence of plastic deformation observed in the cladding in this area.

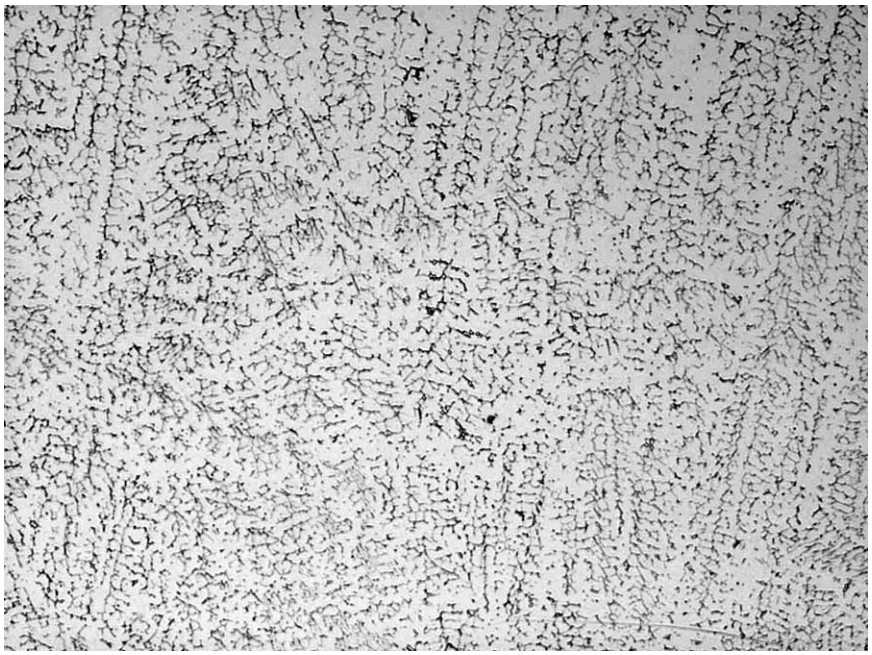

100X

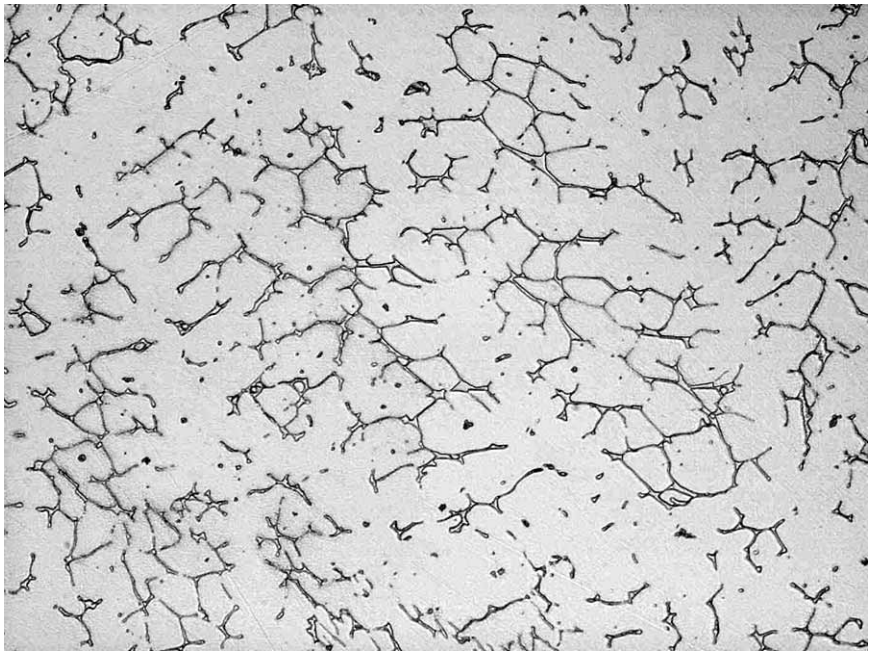

375X

Figure 6.5.1.6: Micrographs showing typical stainless steel cladding microstructure. The dendritic solidification structure is delineated by small pools (or islands) of ferrite in an austenitic matrix.

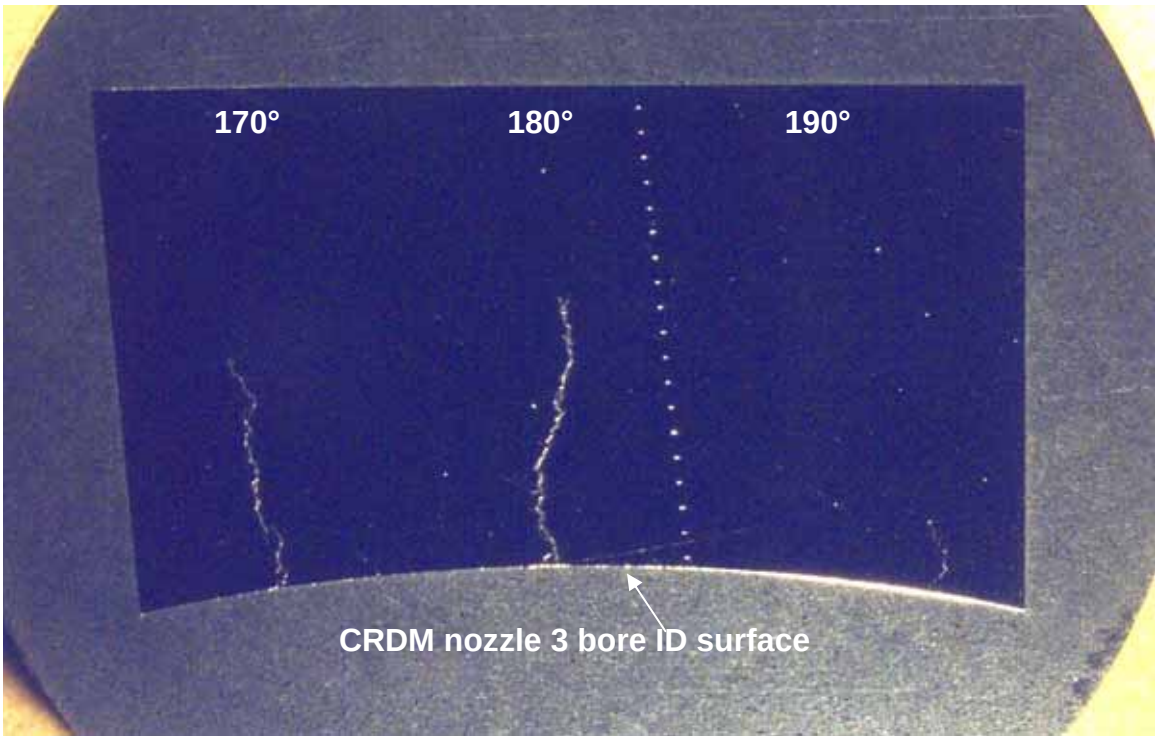

6X

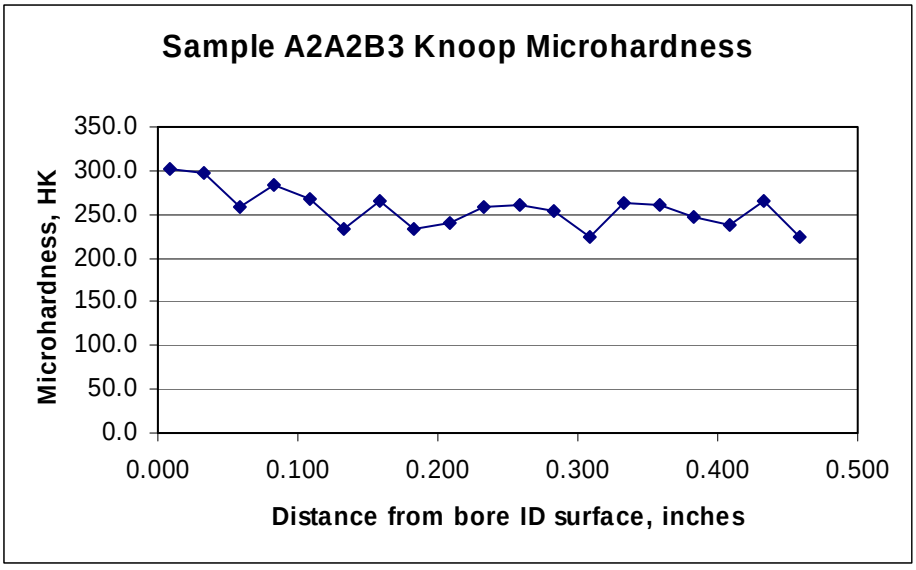

Figure 7.1.1.1: Macro photograph and Knoop microhardness results for metallographic sample A2A2B3 (see Figure 5.2 for the sample orientation). The lower concave surface is the I.D. of the nozzle 3 bore from the nozzle removal process. The crack tips of the two cracks are estimated to be approximately 0.24" and 0.20" below the surface, respectively. The indentations from the microhardness traverse are visible. The elevated microhardness level near the surface is due to the surface cold work layer from the boring of nozzle 3 removal process (see Figures 5.2 and 7.1.1.5).

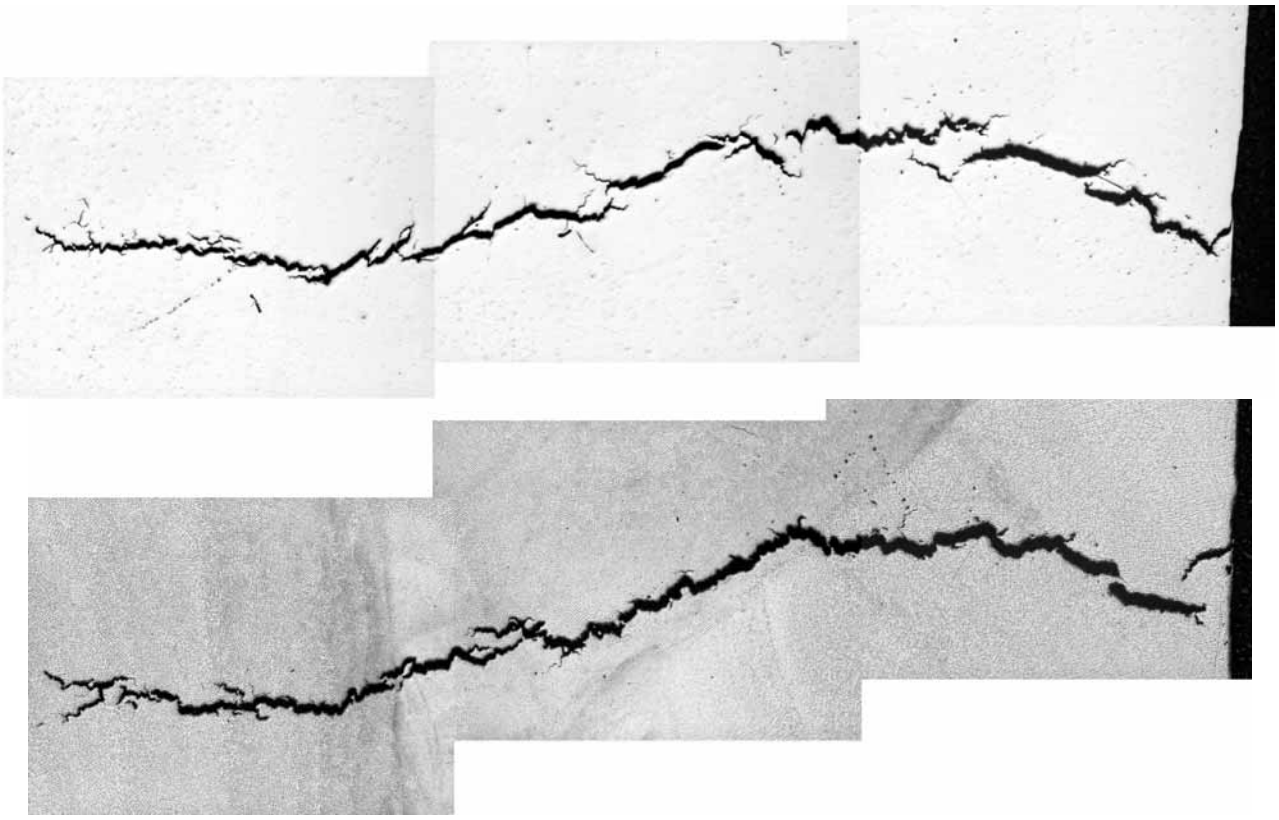

Figure 7.1.1.2: Micrographs showing the crack at ~180^{o} in sample A2A2B3. Top as-polished, bottom etched. Both micrographs 24X.

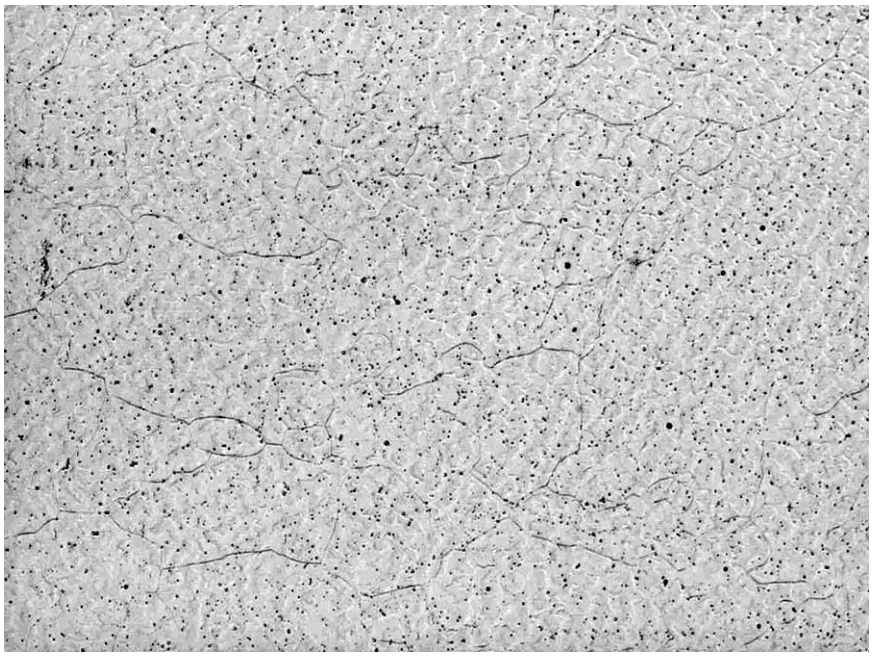

Etched 375X

Figure 7.1.1.3: Typical microstructure of sample A2A2B3. The grain size and dendritic structure within each grain are consistent with typical Alloy 182 weld.

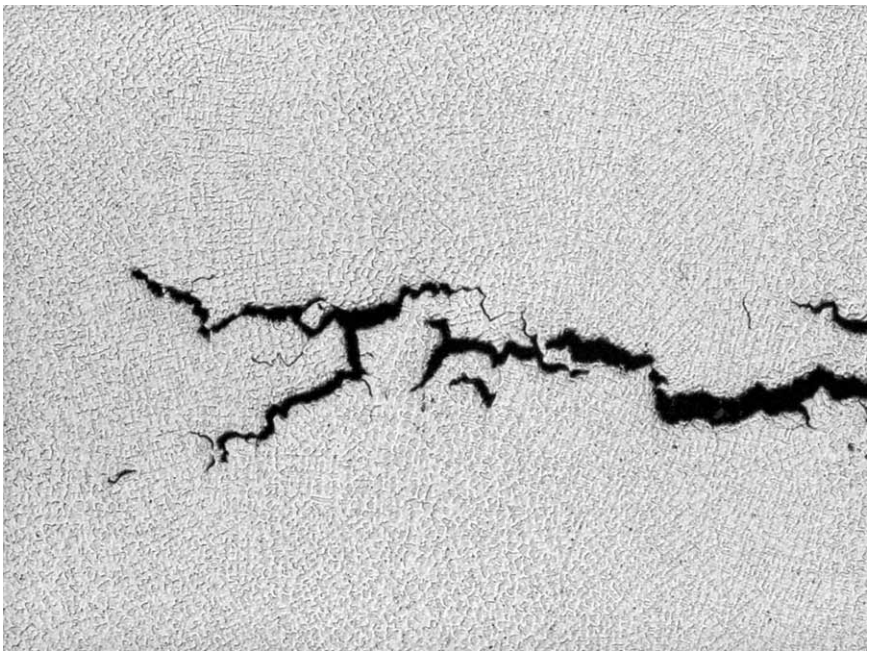

100X

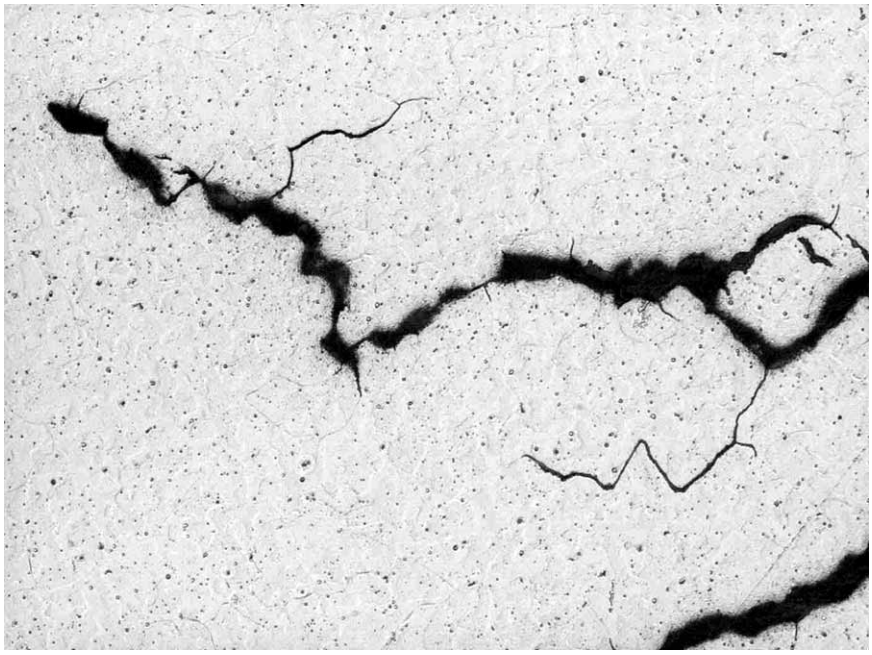

375X

Figure 7.1.1.4: Higher magnification micrographs of the crack tips. Cracking is intergranular or interdendritic.

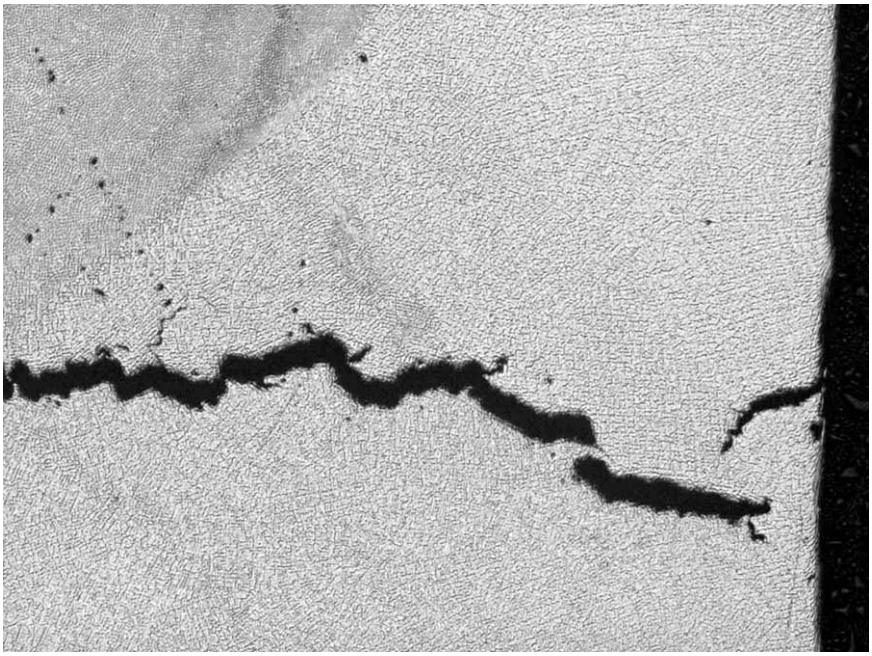

100X

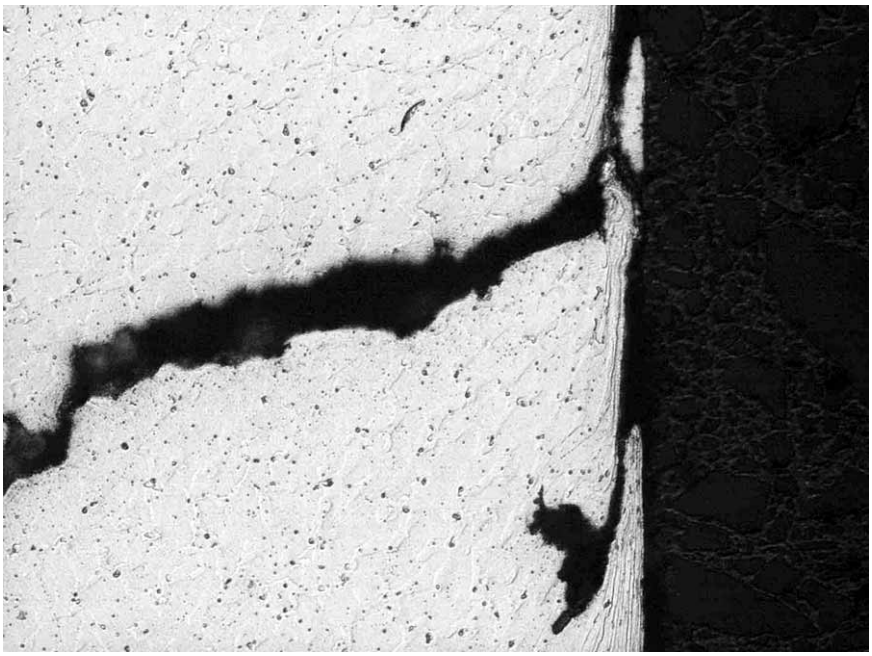

375X

Figure 7.1.1.5: Higher magnification micrographs of the cracking at ~180^{o} near the bored surface. The bored surface shows evidence of surface cold work. The surface cold work is due to the nozzle removal from the RV head and is not related to the J-groove weld fabrication process.

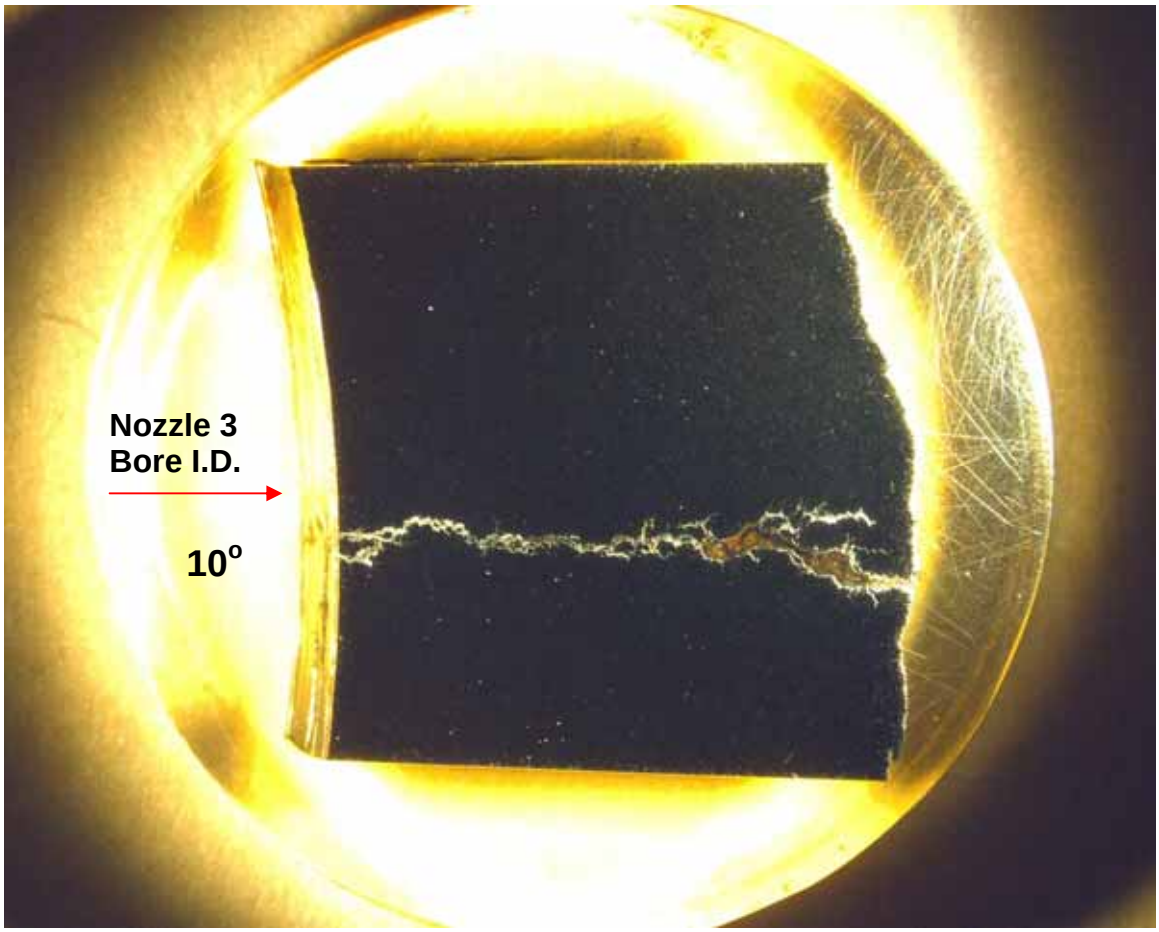

4X

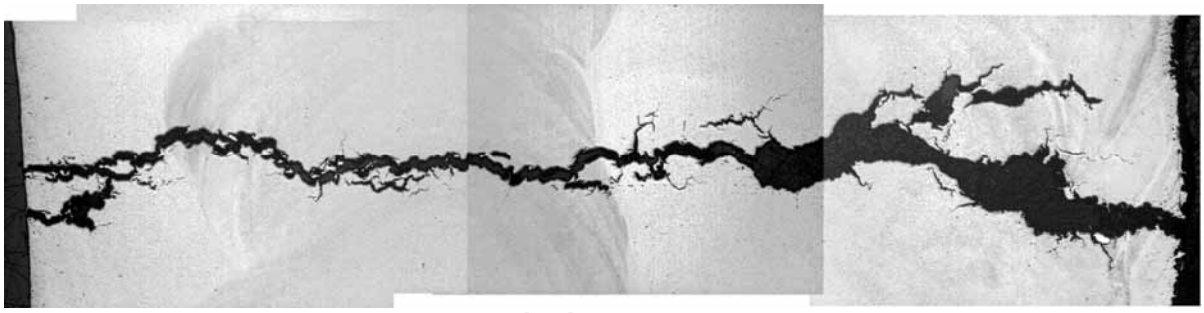

Etched 8X

Figure 7.2.1.1: Macro photograph of metallographic mount sample A2A6B2 (see Figures 5.4 and 5.5 for the sample orientation). The axial cracking at ~10° is through the J-groove weld, in contrast to the cracking near 180°, which was partially through the weld. A slightly higher magnification micrograph is also provided.

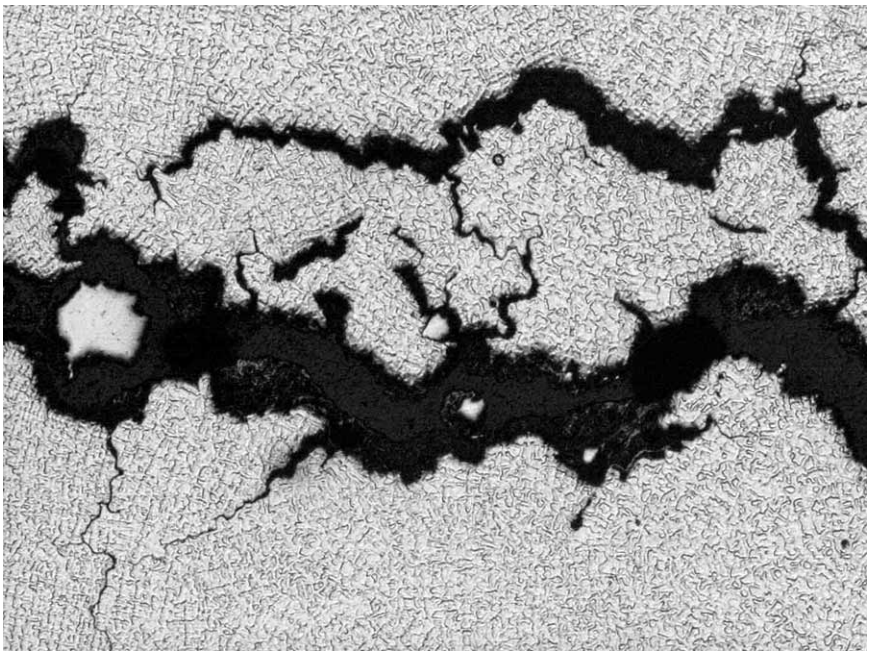

100X

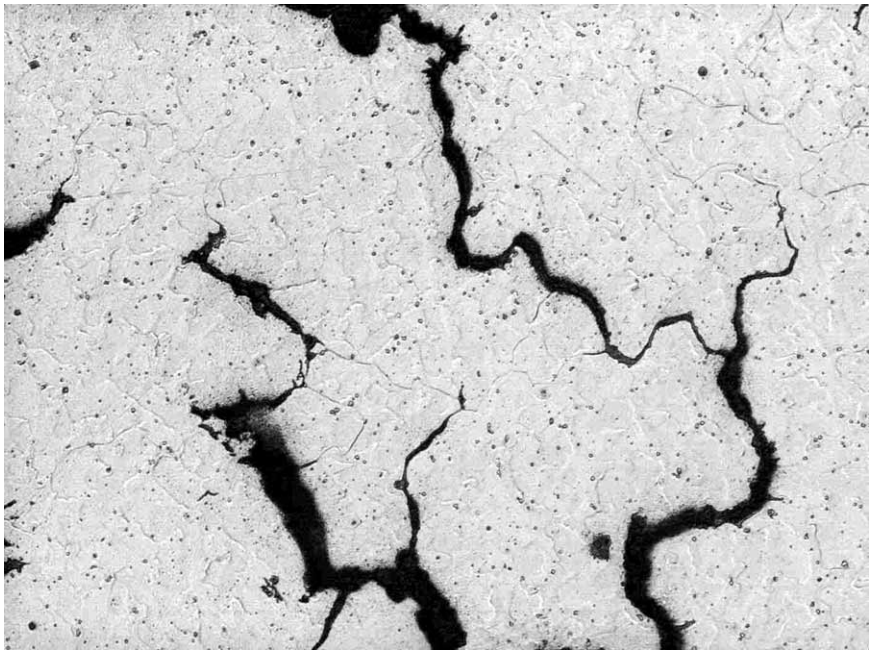

375X

Figure 7.2.1.2: Higher magnification micrographs of the J-groove weld cracking. Cracking is intergranular or interdendritic, similar to the cracking at ~180° in Figure 7.1.1.4.

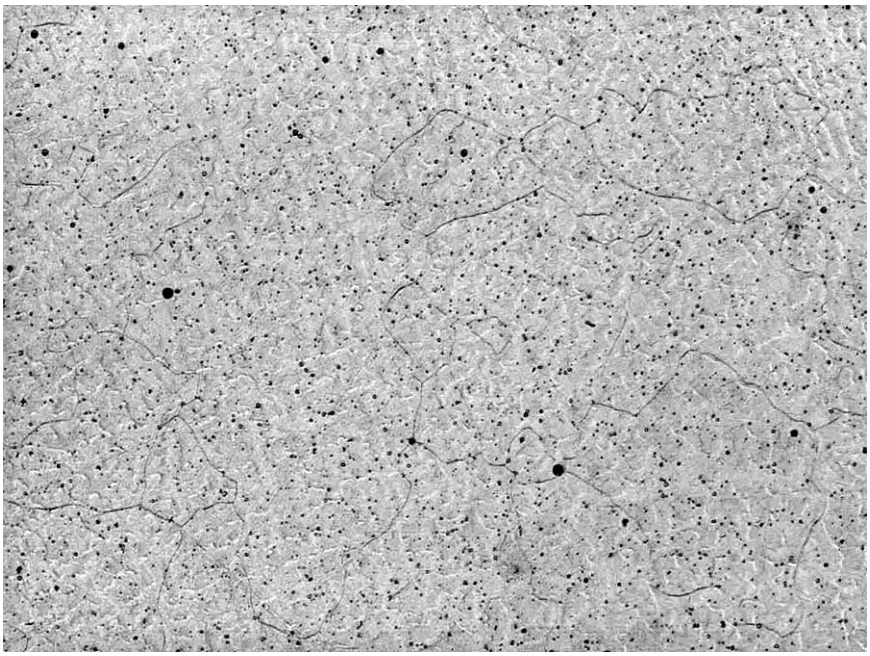

375X

Figure 7.2.1.3: Typical microstructure of sample A2A6B2, which was similar to Figure 7.1.1.3 (at ~180^{o}).

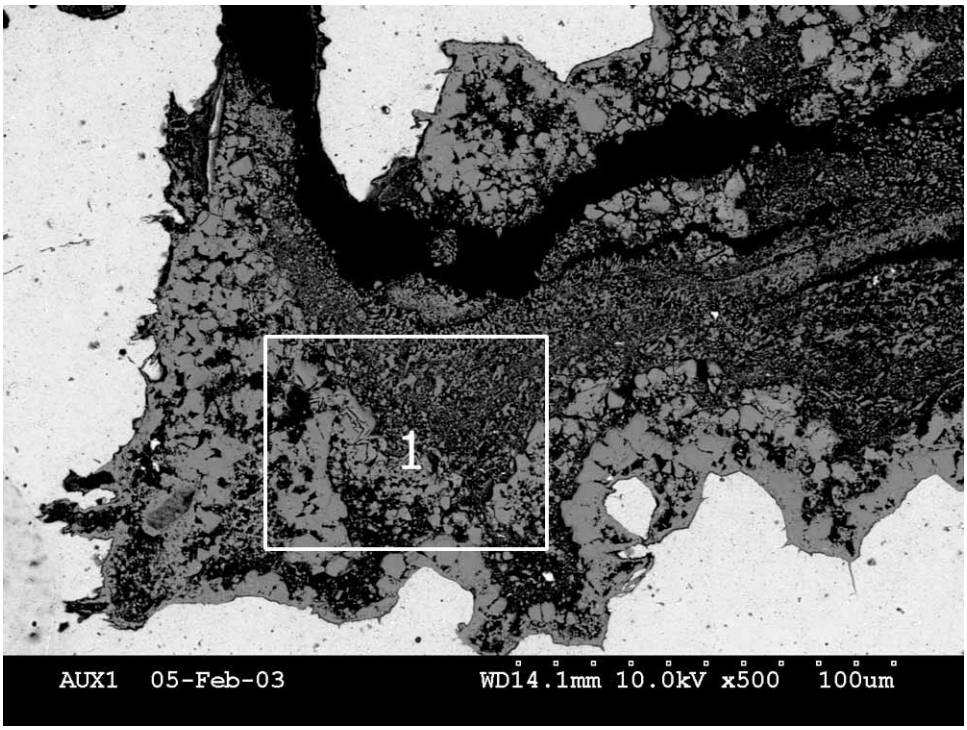

BSE 500X

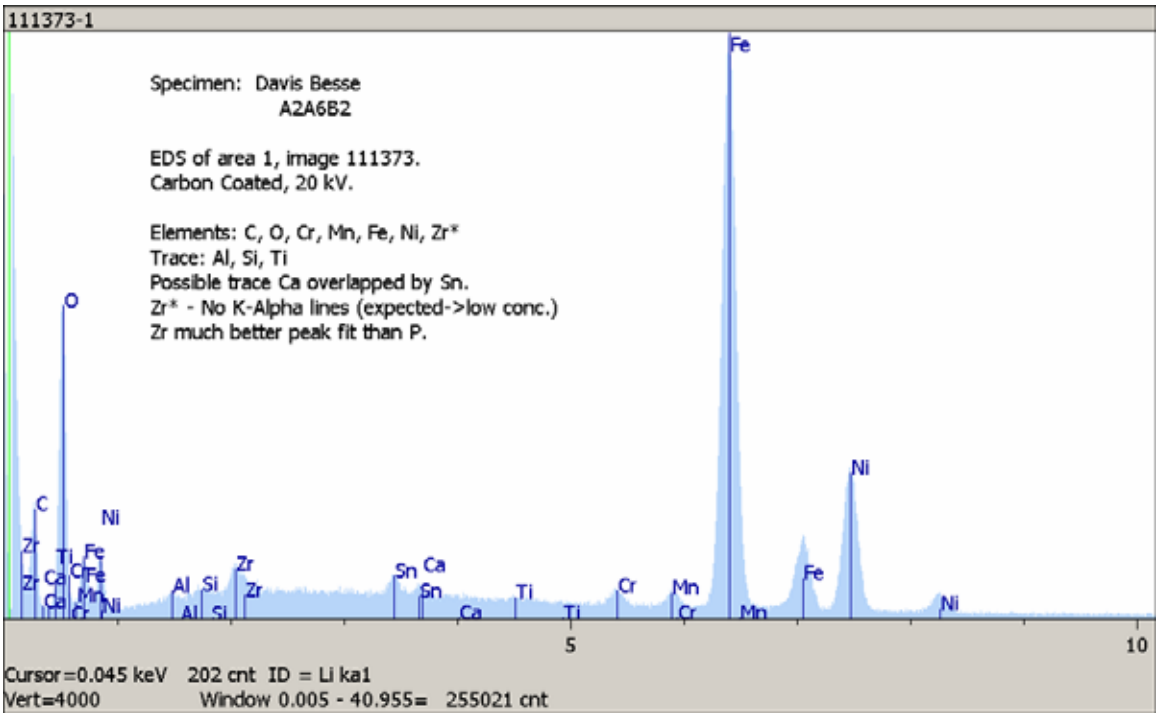

EDS results for area 1 above.

Figure 7.2.2.1: BSE micrograph showing portion of crack filled with corrosion products. The EDS results indicated high concentrations of carbon, oxygen, iron, and nickel.

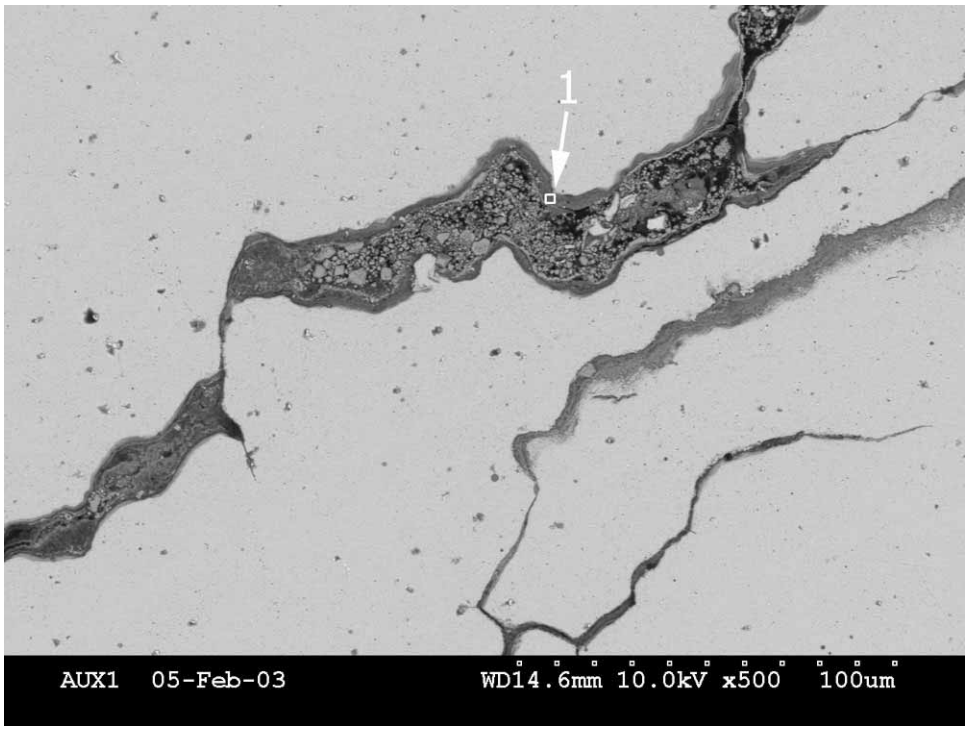

BSE 500X

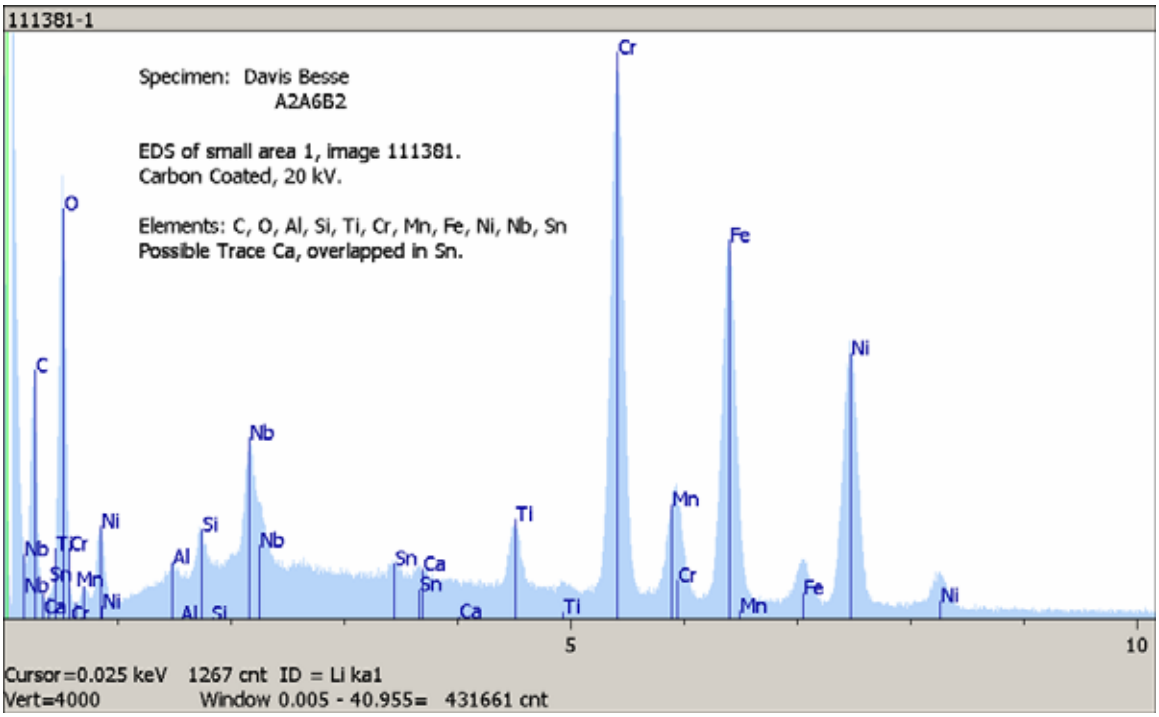

EDS results for area 1 above.

Figure 7.2.2.2: BSE micrograph showing corrosion products near crack tip. The EDS results collected from the area 1 indicated high concentrations of carbon, oxygen, niobium, titanium, chromium, manganese, iron, and nickel.

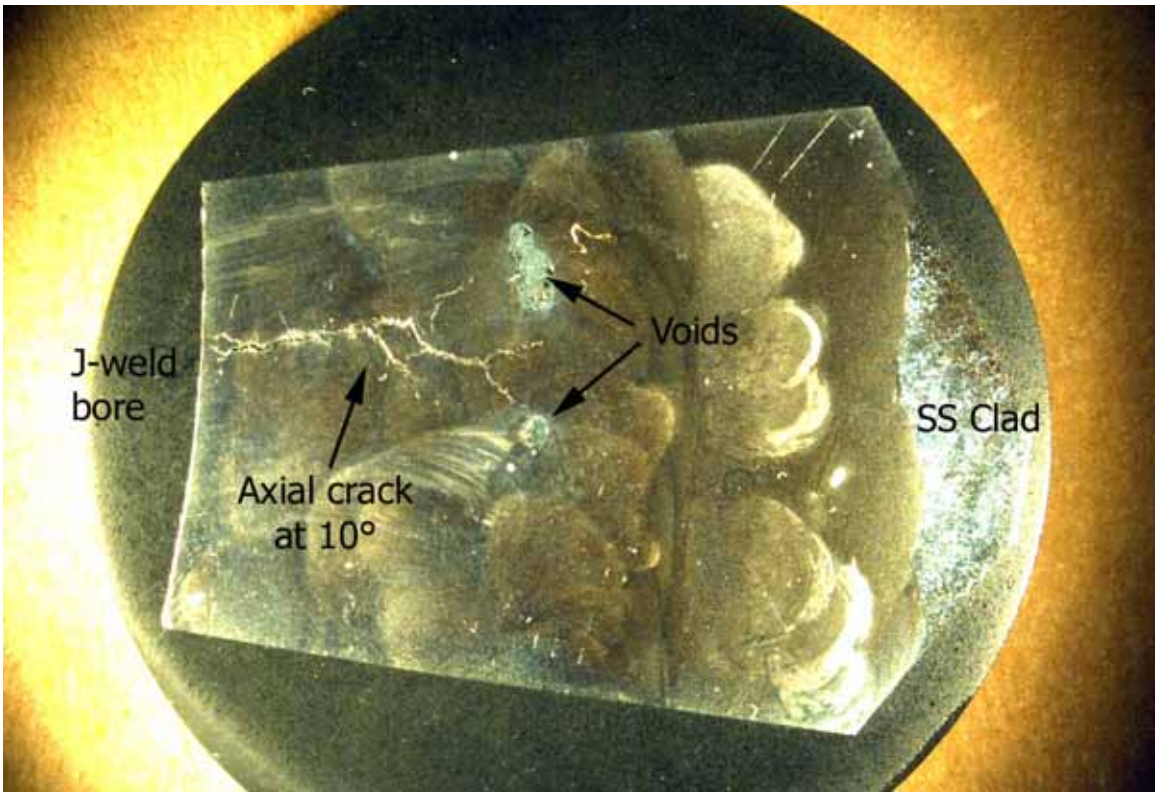

4X

Figure 7.2.3.1: Macro photograph of metallographic mount A2A6A2E1 (see Figure 5.6 and 5.10 for the sample orientation). Cracking was partially through the J-groove weld in the sample plane.

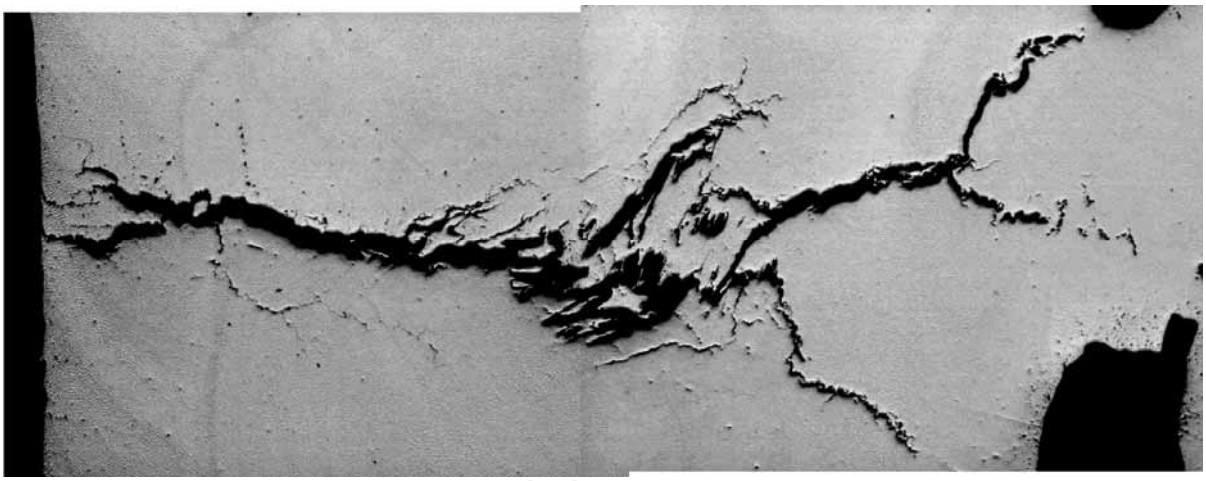

Etched 13X

Figure 7.2.3.2: Micrograph showing axial cracks in the lower portion of the J-groove weld at ~10°. The crack maximum depth is approximately 0.45" beneath the bore I.D. surface.

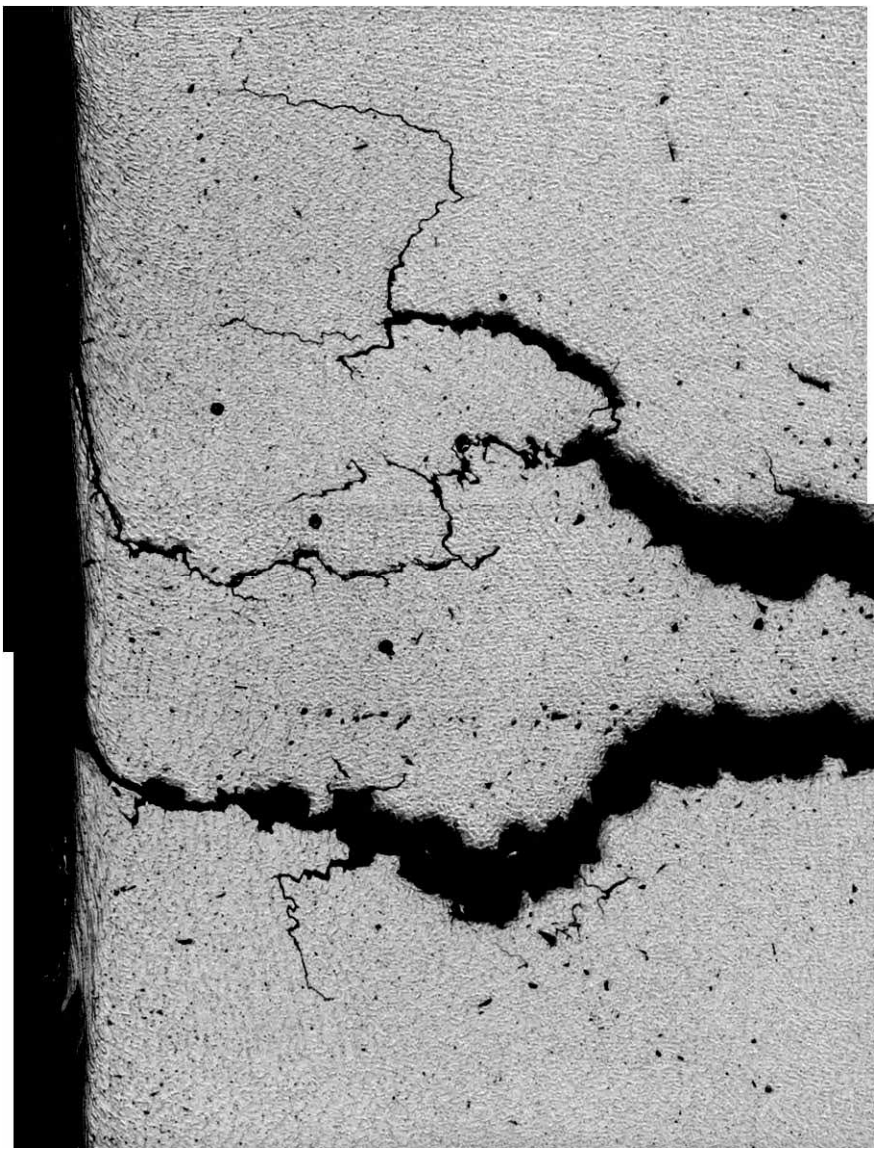

Etched 100X

Figure 7.2.3.3: Cracks located near the bored surface. Surface cold work layer is due to the boring (nozzle removal) process.

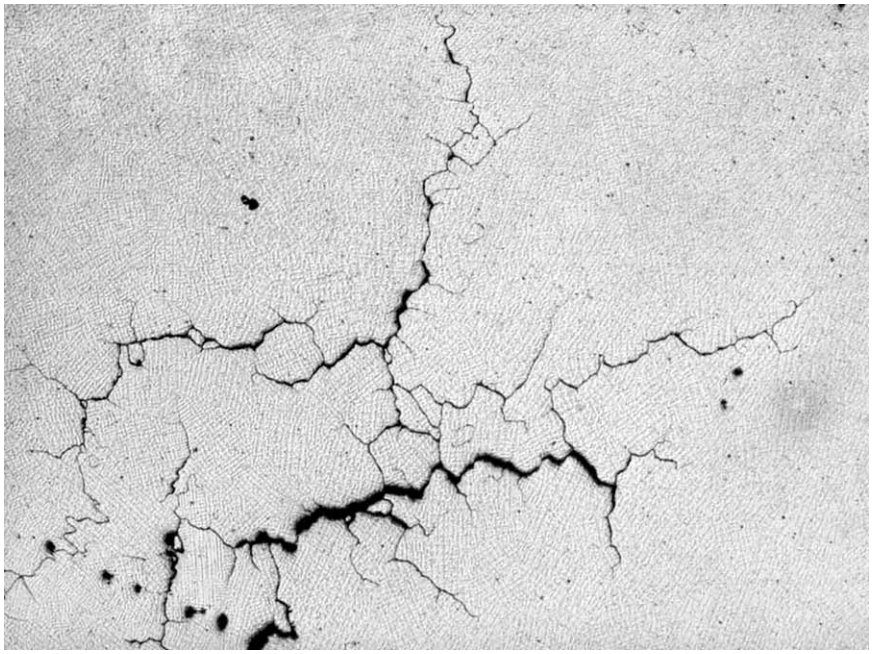

Etched 100X

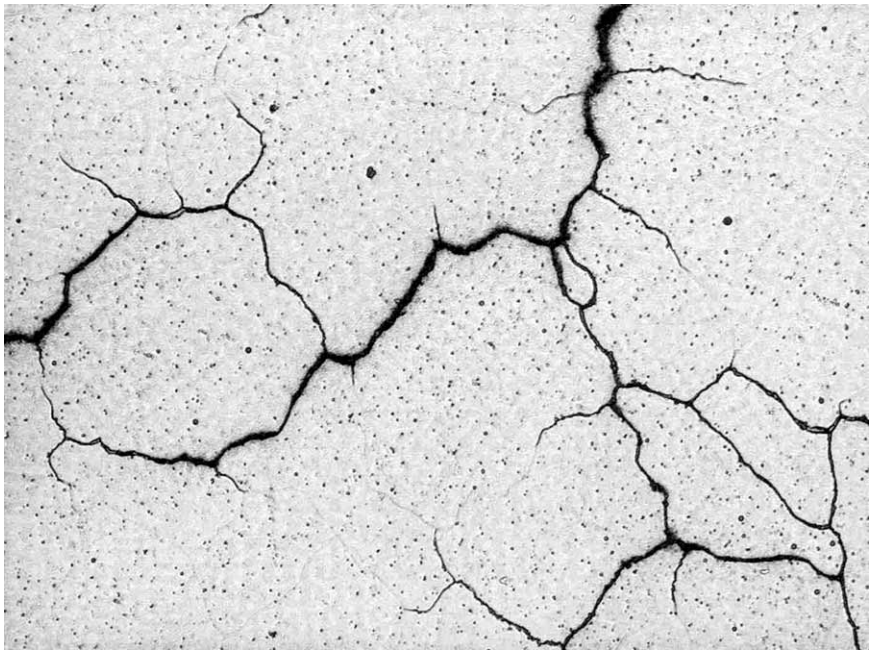

Etched 375X

Figure 7.2.3.4: Interdendritic or intergranular cracking in the J-groove weld away from the bore I.D. surface.

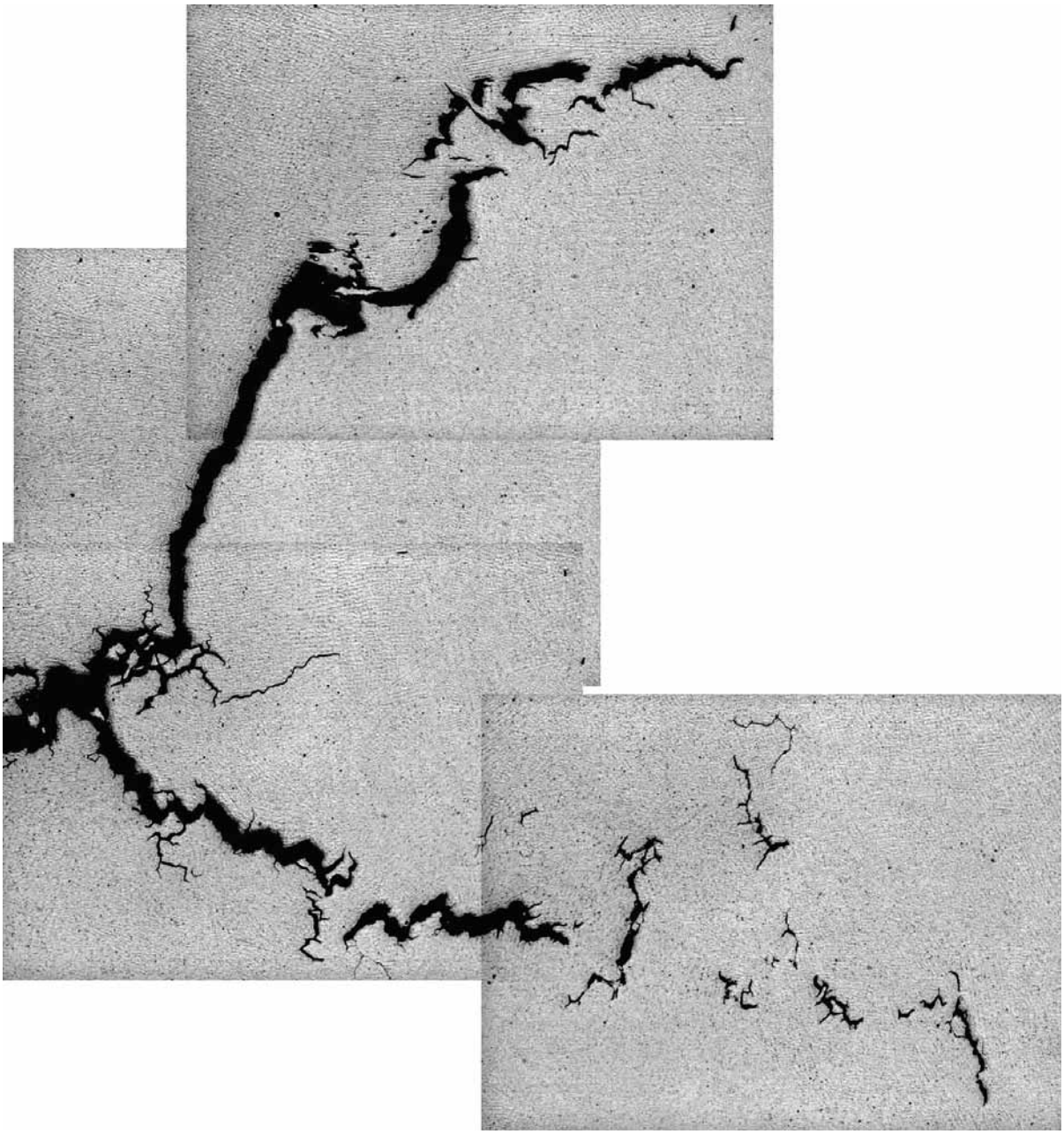

Etched 77X

Figure 7.2.3.5: Crack tips toward the J-groove weld O.D.

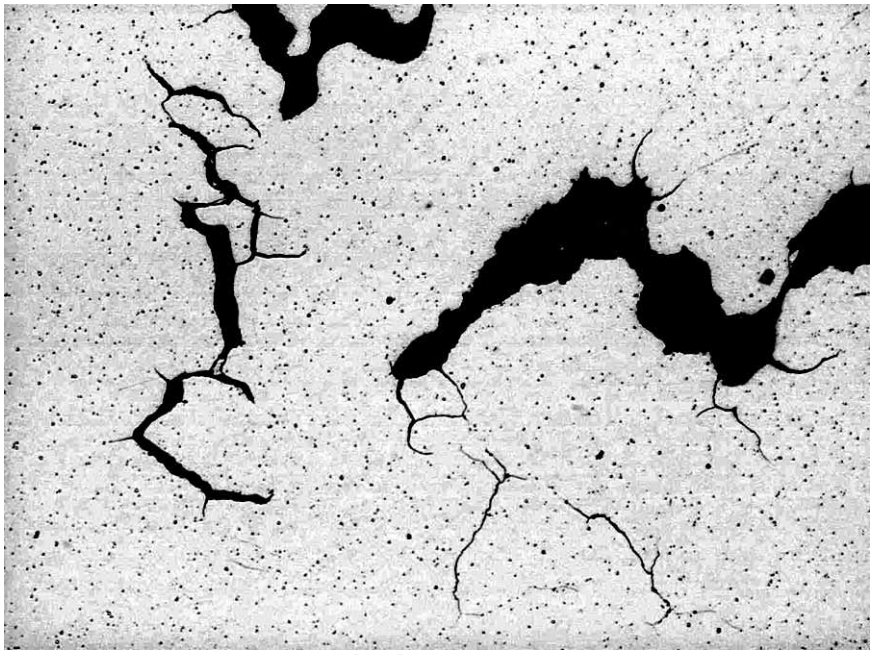

Etched 375X

Figure 7.2.3.6: Crack detail from Figure 7.2.3.5.

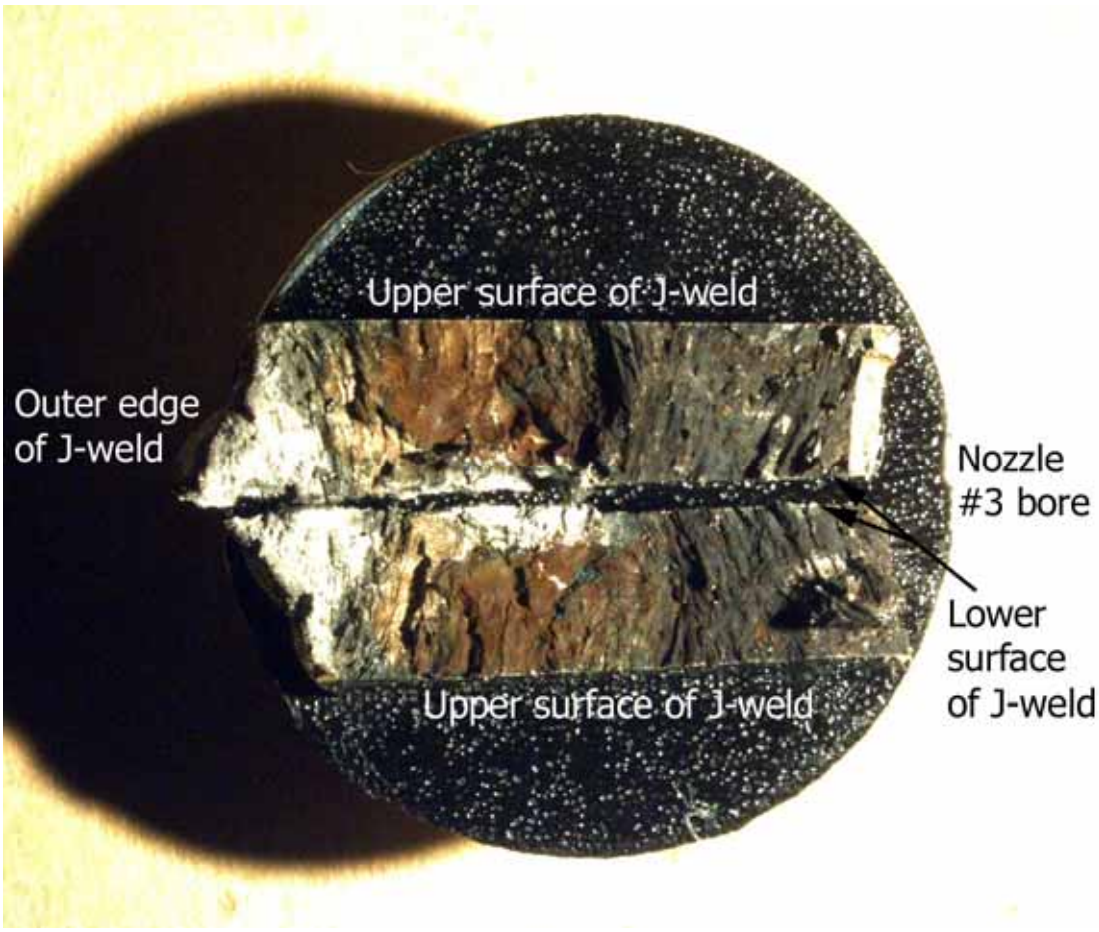

4X

Figure 7.2.4.1: Macro photograph of sample A2A6B3 with the middle portion of the axial cracking at ~10° opened-up for SEM. Refer to Figures 5.4 and 5.5 for the sample location.

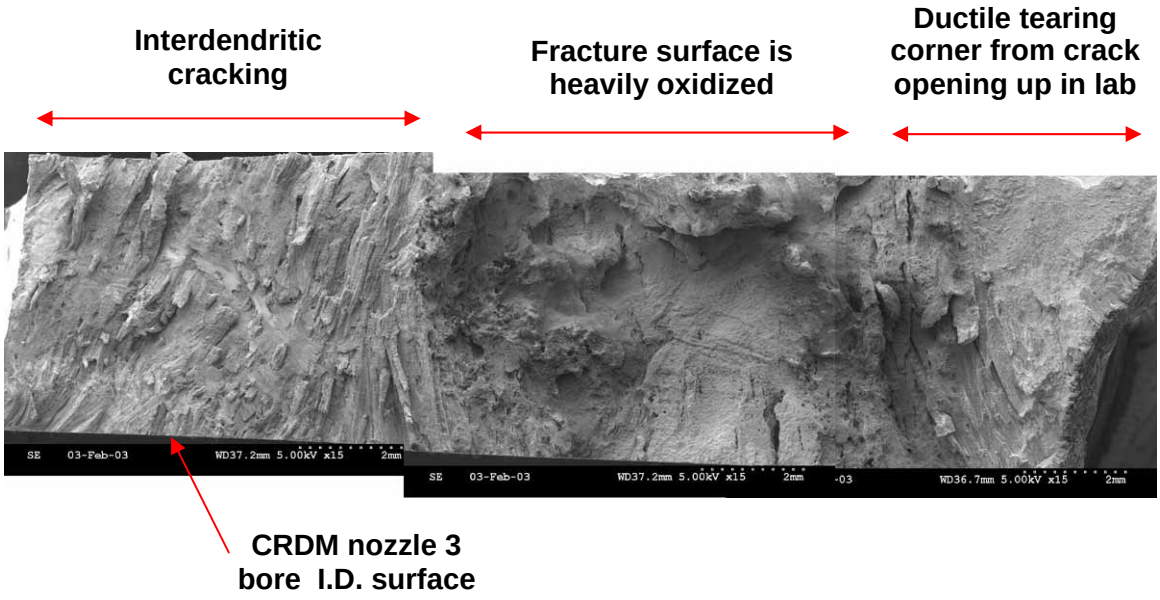

Figure 7.2.4.2: Low magnification SEM mosaic of the fracture surface after opening-up the axial crack. BSE 6.7X

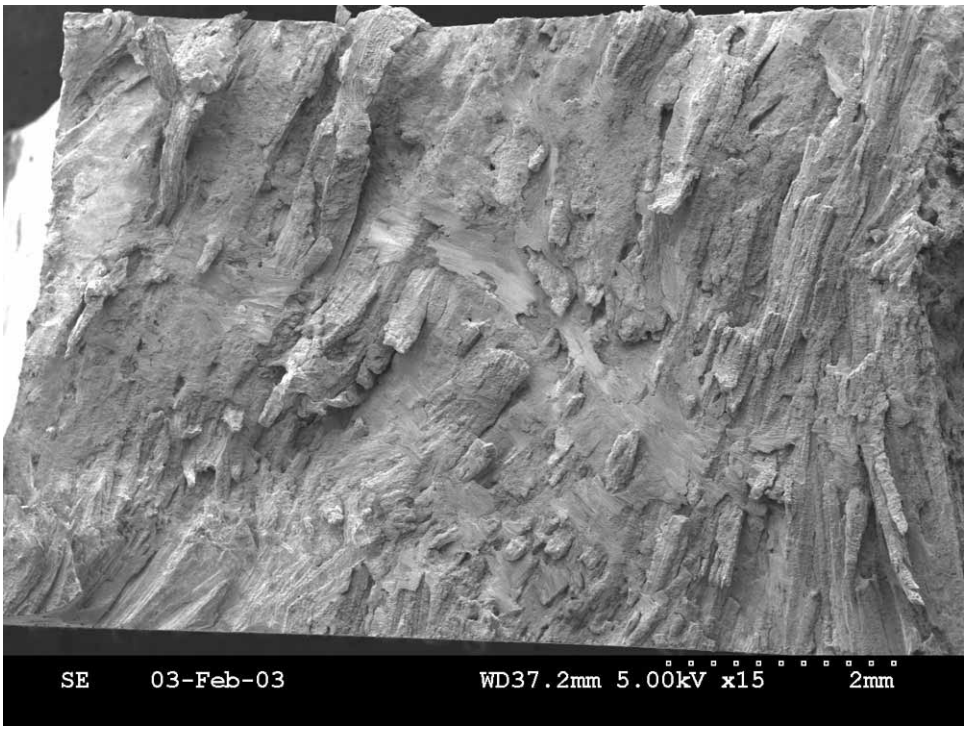

Figure 7.2.4.3: Higher magnification of the left section in Figure 7.2.4.2. Cracking is interdendritic exposing a well-defined columnar solidification structure.

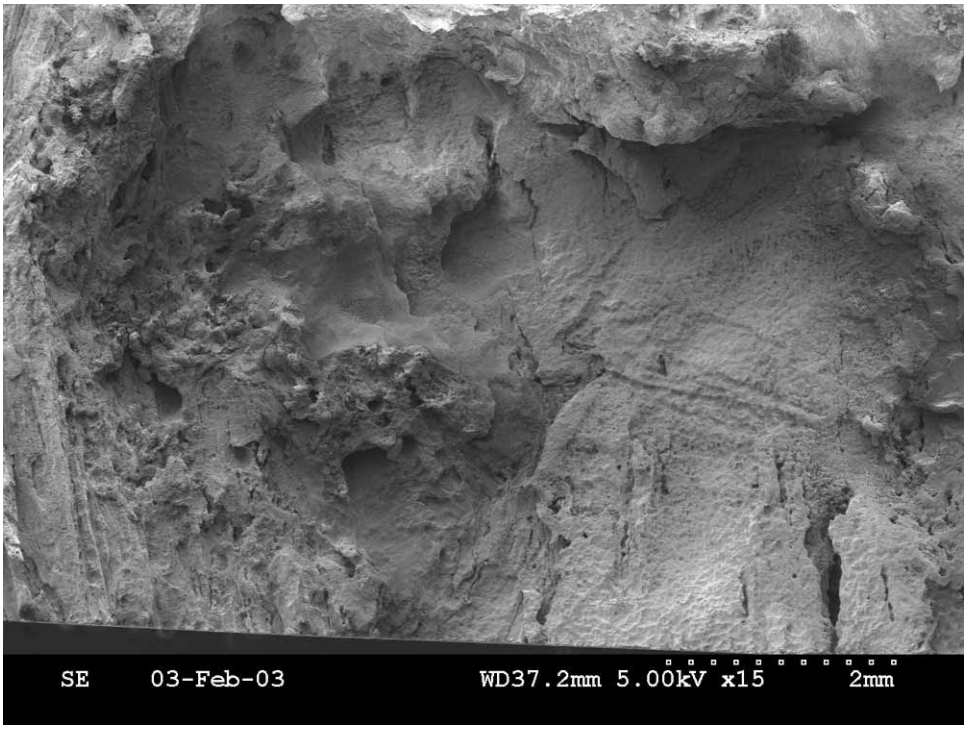

Figure 7.2.4.4: Higher magnification of the middle section in Figure 7.2.4.2. The fracture surface is heavily oxidized; the fracture mode is indeterminate.

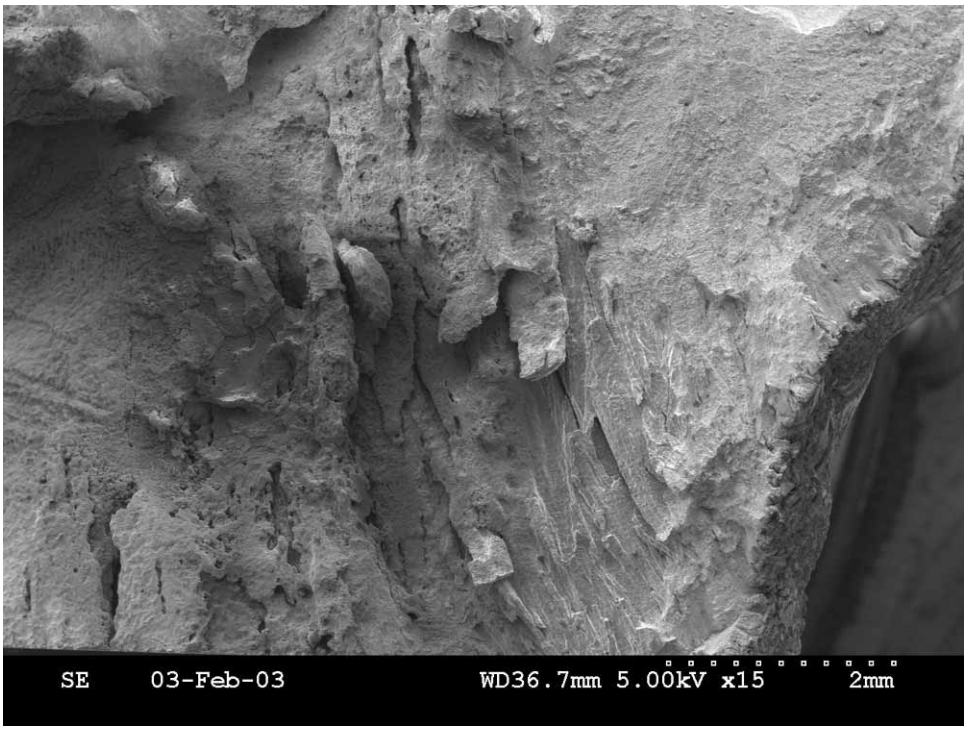

Figure 7.2.4.5: Higher magnification of the right section in Figure 7.2.4.2. Cracking to the left side of ductile tearing (lab fracture) is interdendritic.

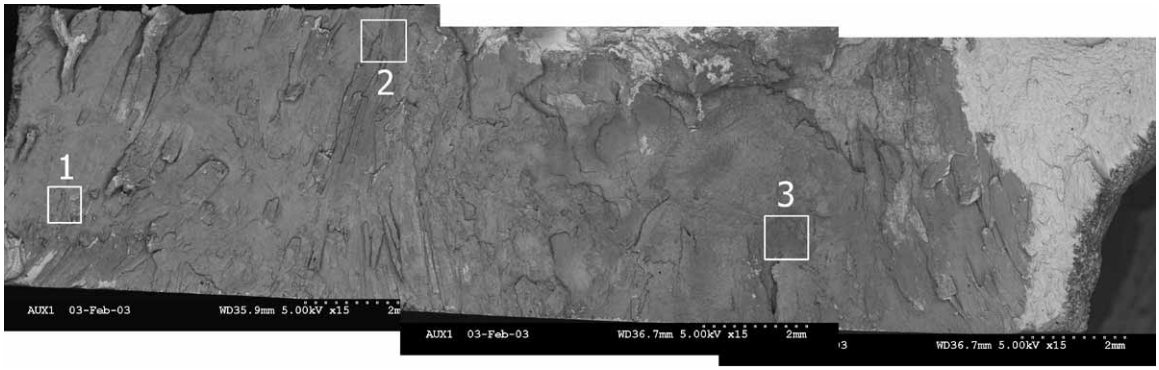

BSE 6.7X

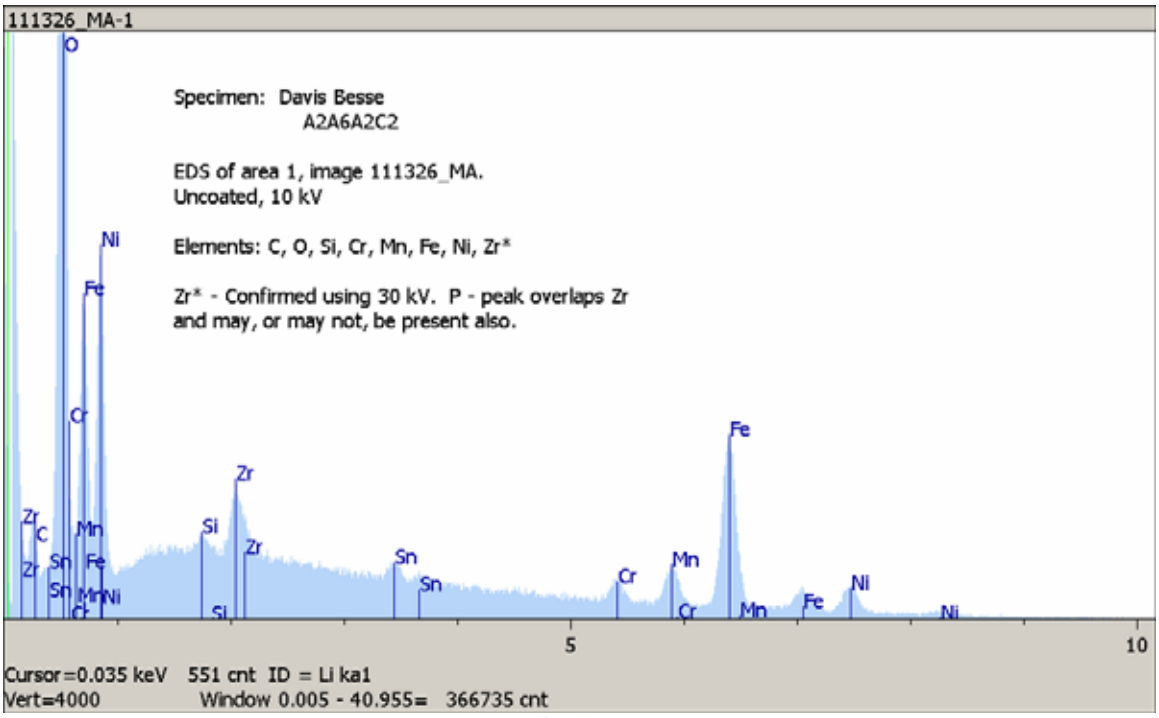

EDS results for area 1.

Figure 7.2.4.6: BSE micrograph mosaic of the open crack surface (same area as Figure 7.2.4.2) along with EDS results for three areas of the fracture surface. The dark area in the BSE image indicates the fracture surface was covered by a thick oxide layer. The light area (right side) indicates a fresh fracture surface due to crack opening-up (i.e., less oxide on surface). For area 1, the primary elements included carbon, oxygen, silicon, chromium, manganese, iron, nickel, and zirconium.

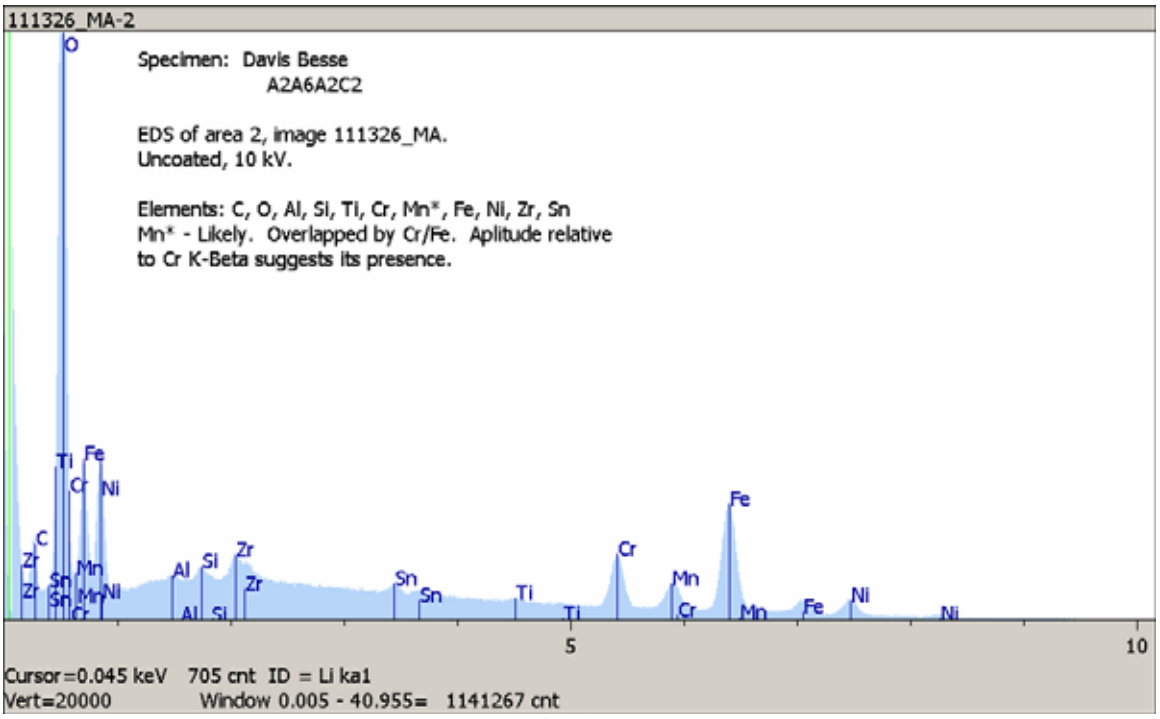

EDS results for area 2.

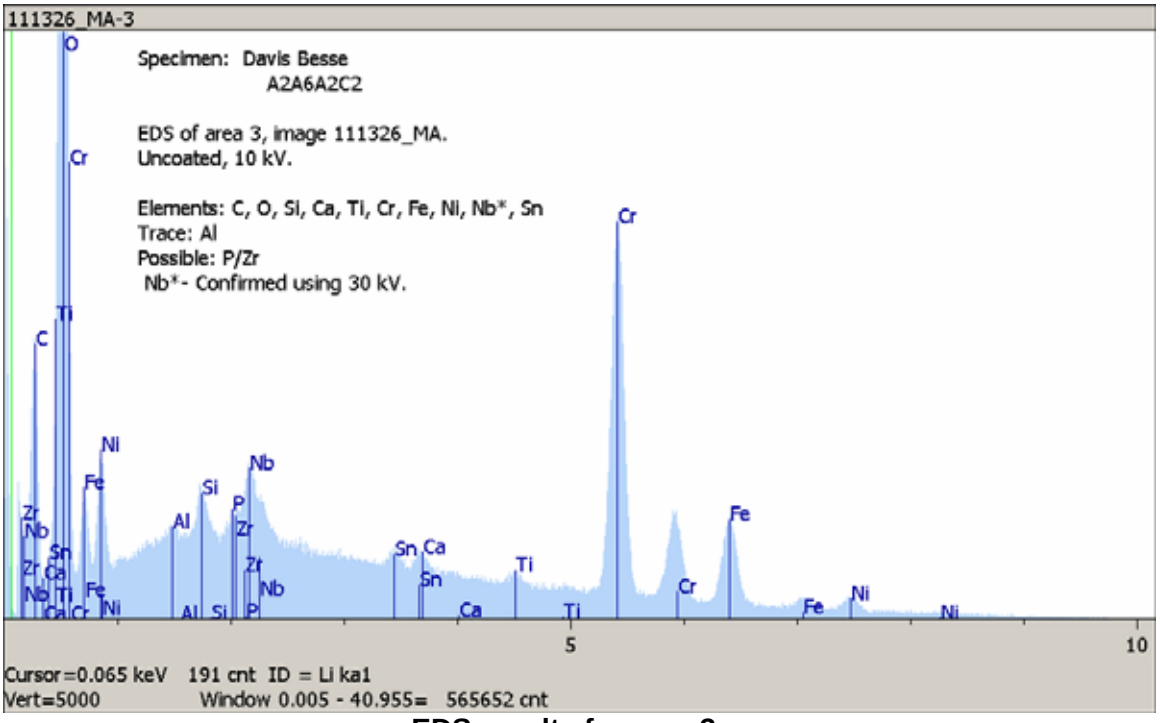

EDS results for area 3.

Figure 7.2.4.6 (cont.): For area 2, the primary elements included carbon, oxygen, silicon, chromium, manganese, iron, nickel, and zirconium. Similar results were obtained for area 3, except area 3 also contained niobium and calcium.

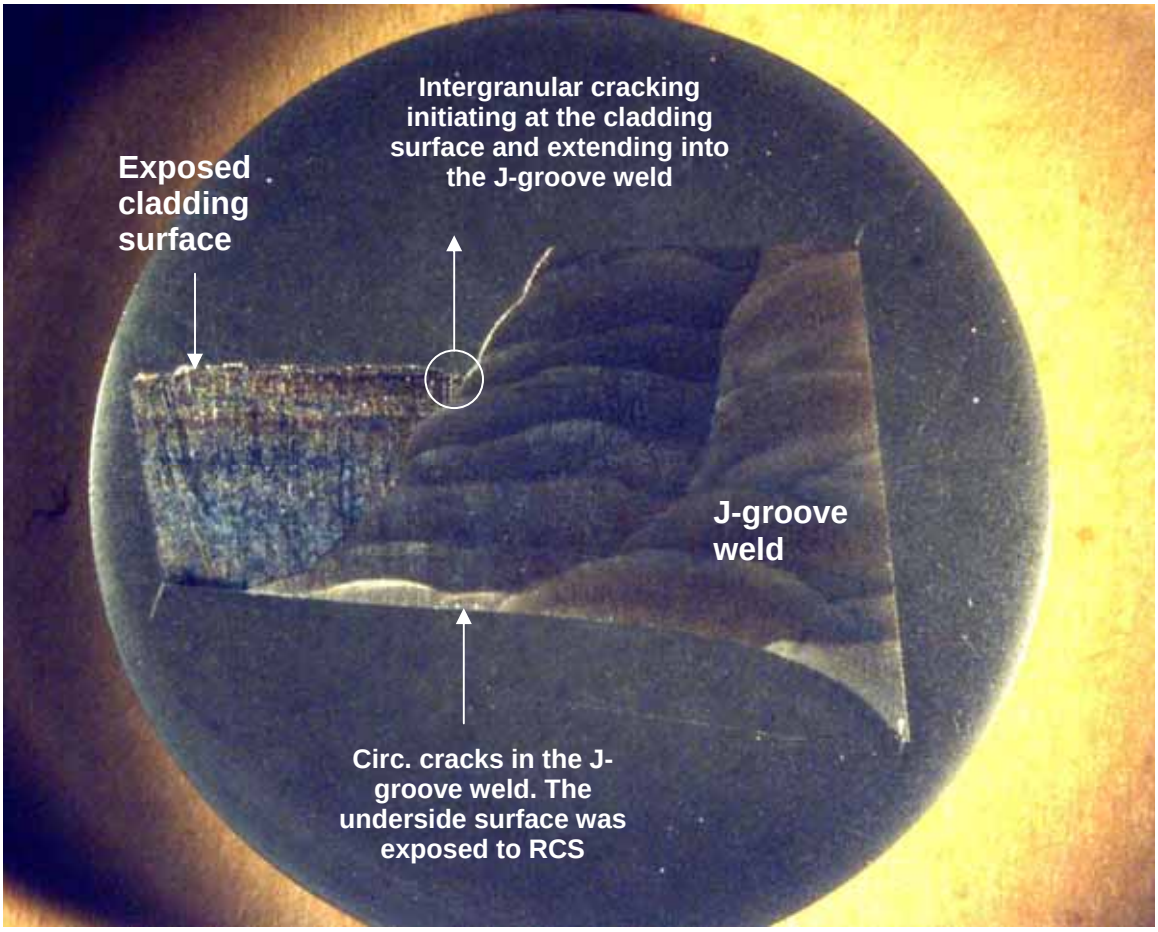

Figure 7.3.1.1: Macro photograph of metallographic sample A2A6A2B2. The mounted surface is through the J-groove weld at ~45°. Refer to Figures 5.6 and 5.7 for the sample orientation.

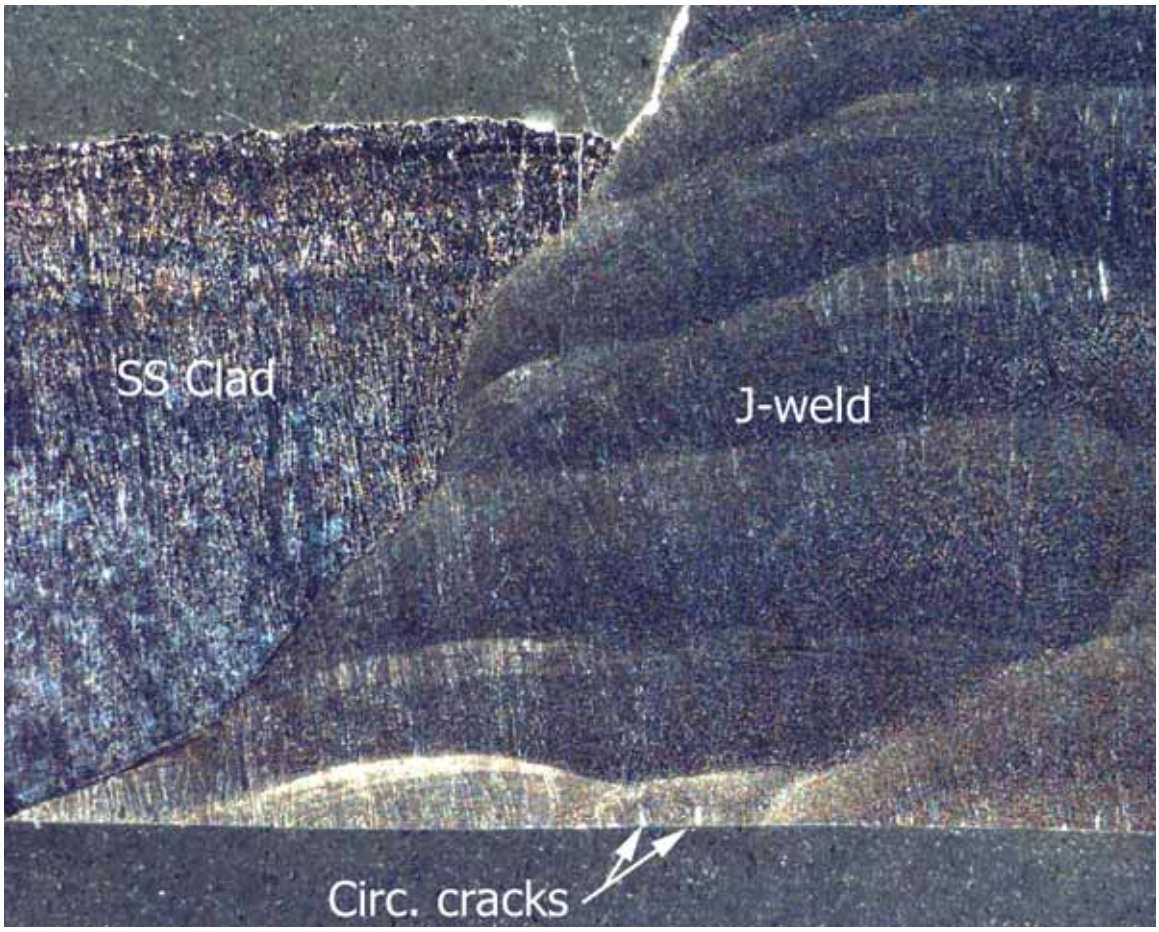

12X

Figure 7.3.1.2: Slightly higher magnification photograph of metallographic mount A2A6A2B2.

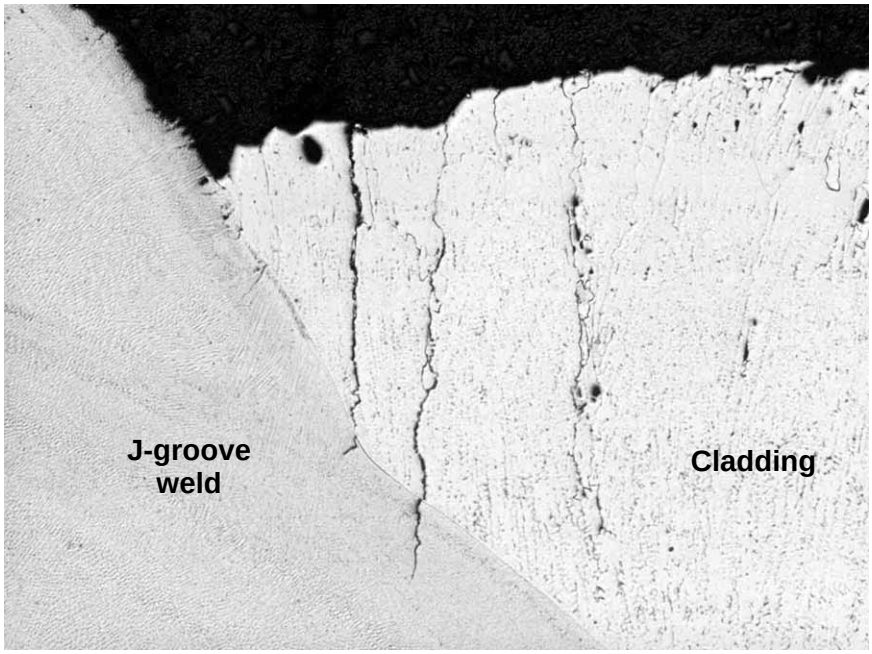

Etched 48X

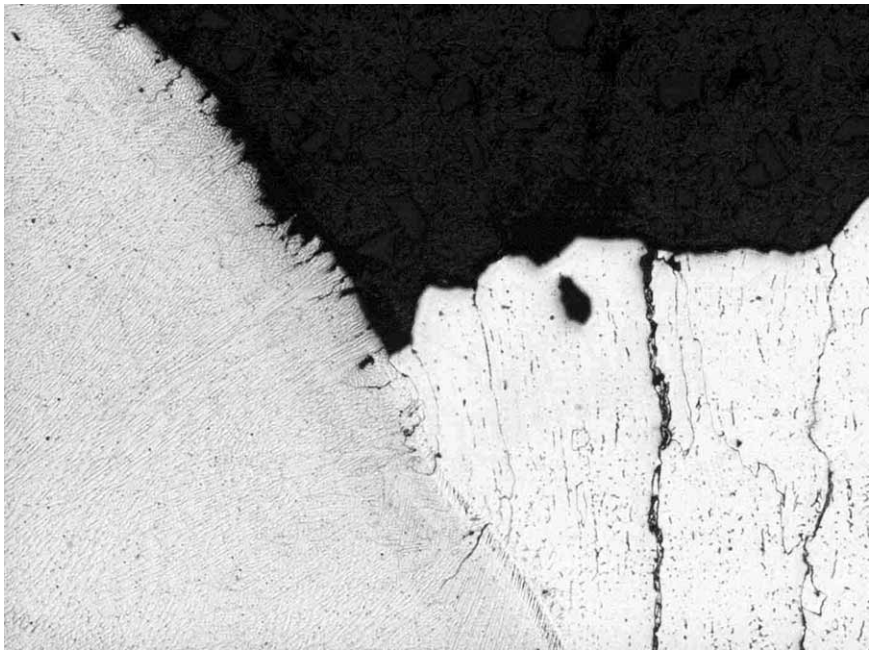

Etched 100X

Figure 7.3.1.3: Intergranular or interdendritic cracking initiating at the cladding surface and extending into the J-groove weld. Note that the micrographs shown are mirror image of the photo in Figure 7.3.1.2. Intergranular attack (IGA) is also evident on the exposed surface of J-groove weld and cladding (surface exposed to oxygenated boric acid). This cracking is likely initiated by IGA.

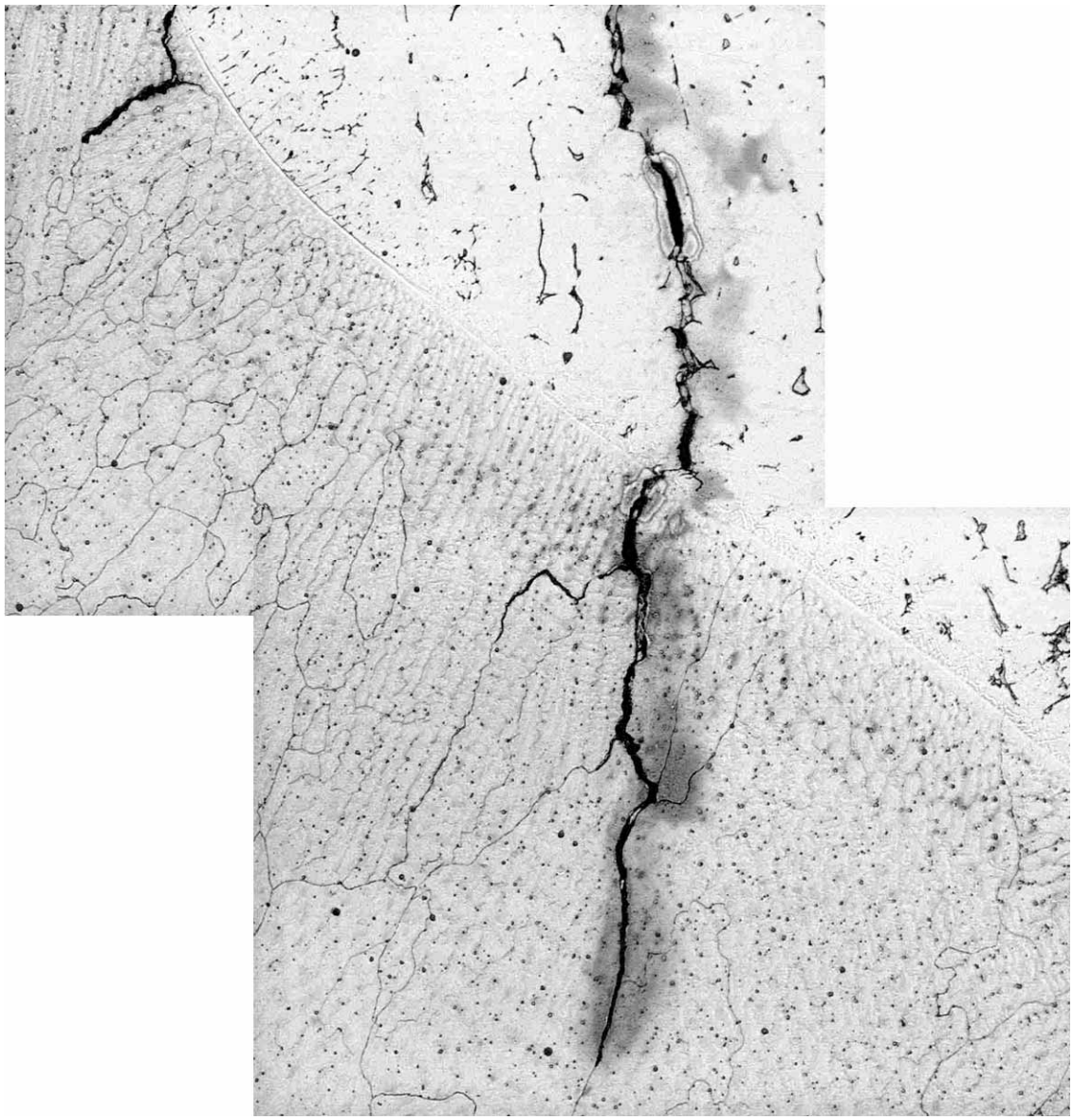

Etched 375X

Figure 7.3.1.4: Higher magnification micrograph showing intergranular or interdendritic cracking initiating at the cladding surface and extending into the J-groove weld.

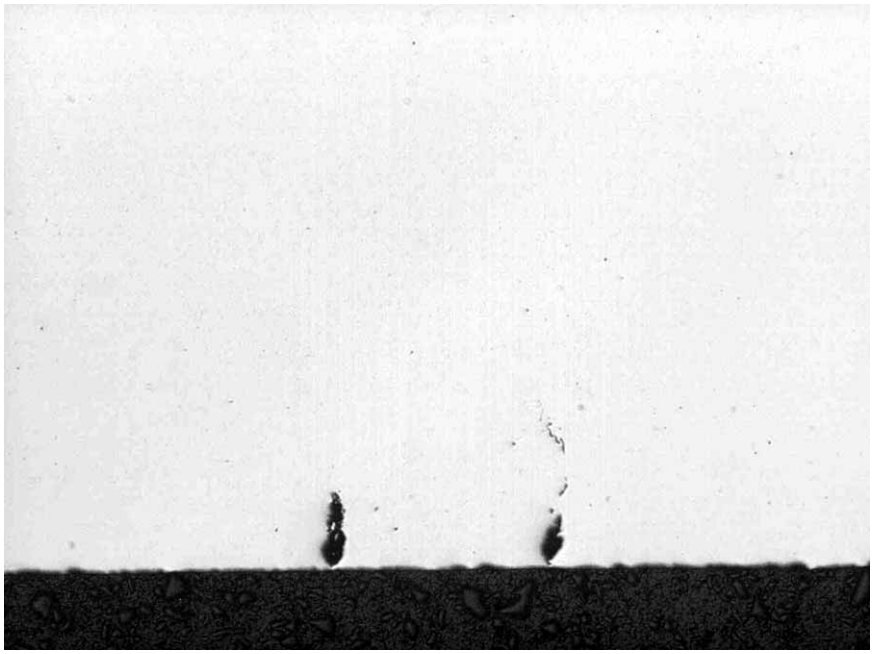

As-polished 48X

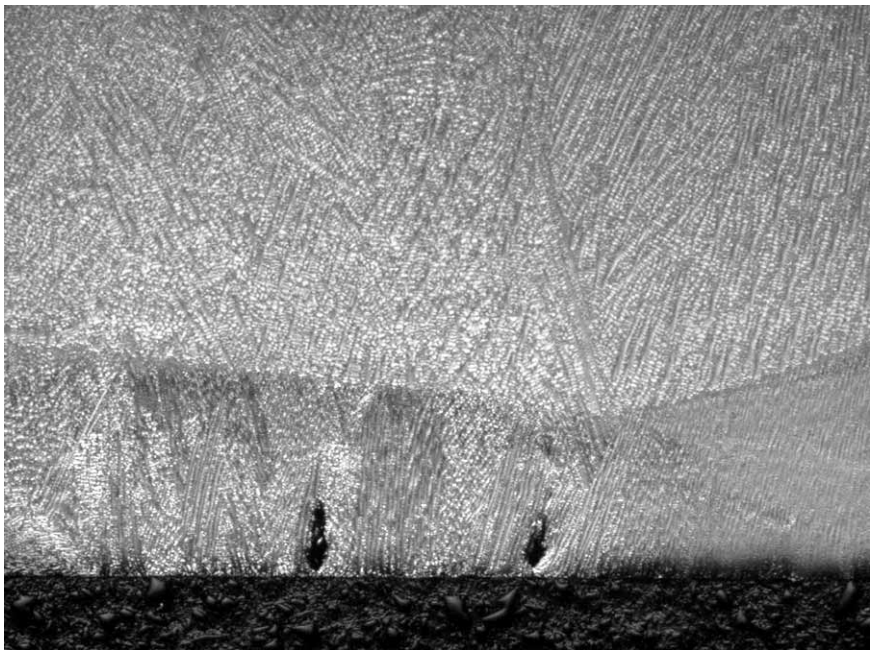

Etched 48X

Figure 7.3.1.5: Low magnification micrographs showing shallow circumferential cracking in the J-groove weld.

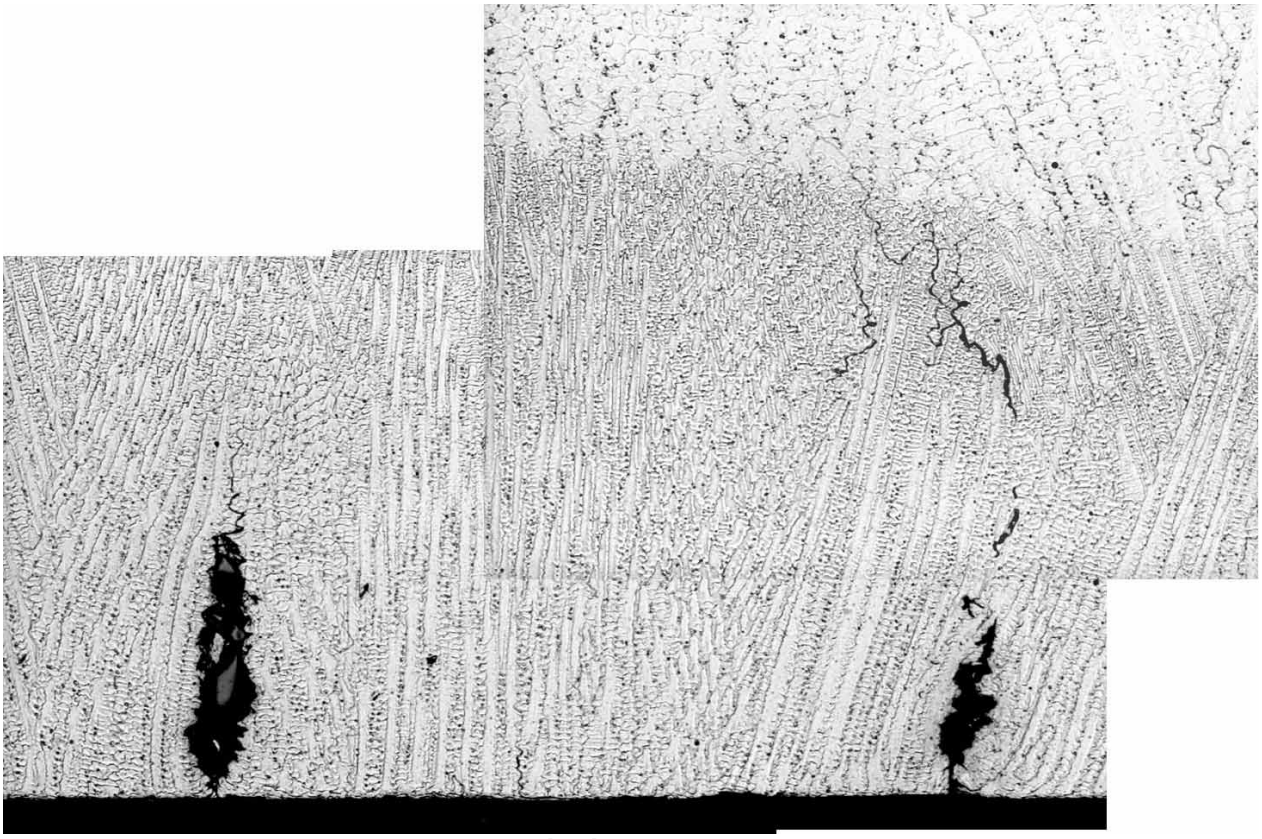

Etched 170X

Figure 7.3.1.6: Micrograph showing the shallow circumferential cracks in the J-groove weld. The cracking is intergranular or interdendritic, with a maximum depth of approximately 0.019" below the surface. The two wider crack regions just below the surface may have been dendrites or grains encircled by cracks that subsequently dropped out during sample preparation.

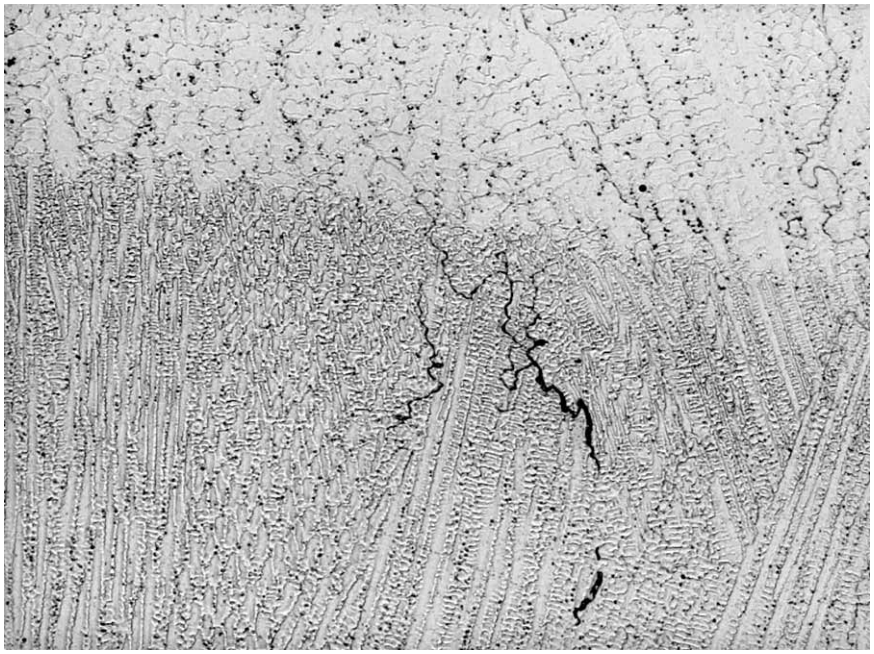

Etched 190X

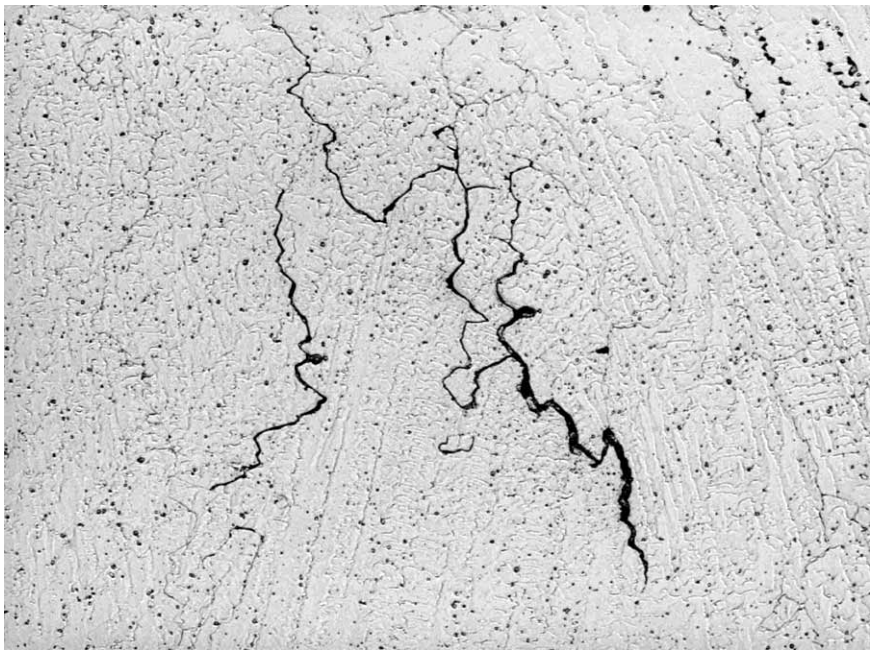

Etched 375X

Figure 7.3.1.7: Micrographs showing crack tips of the circumferential cracking in the J-groove weld.

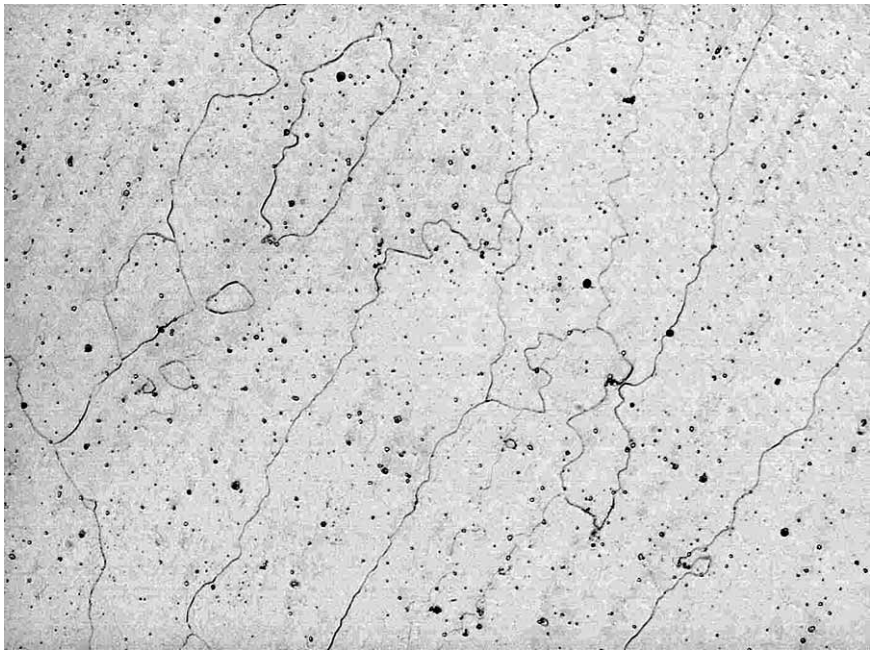

Etched 375X

Figure 7.3.1.8: Typical J-groove weld microstructure.

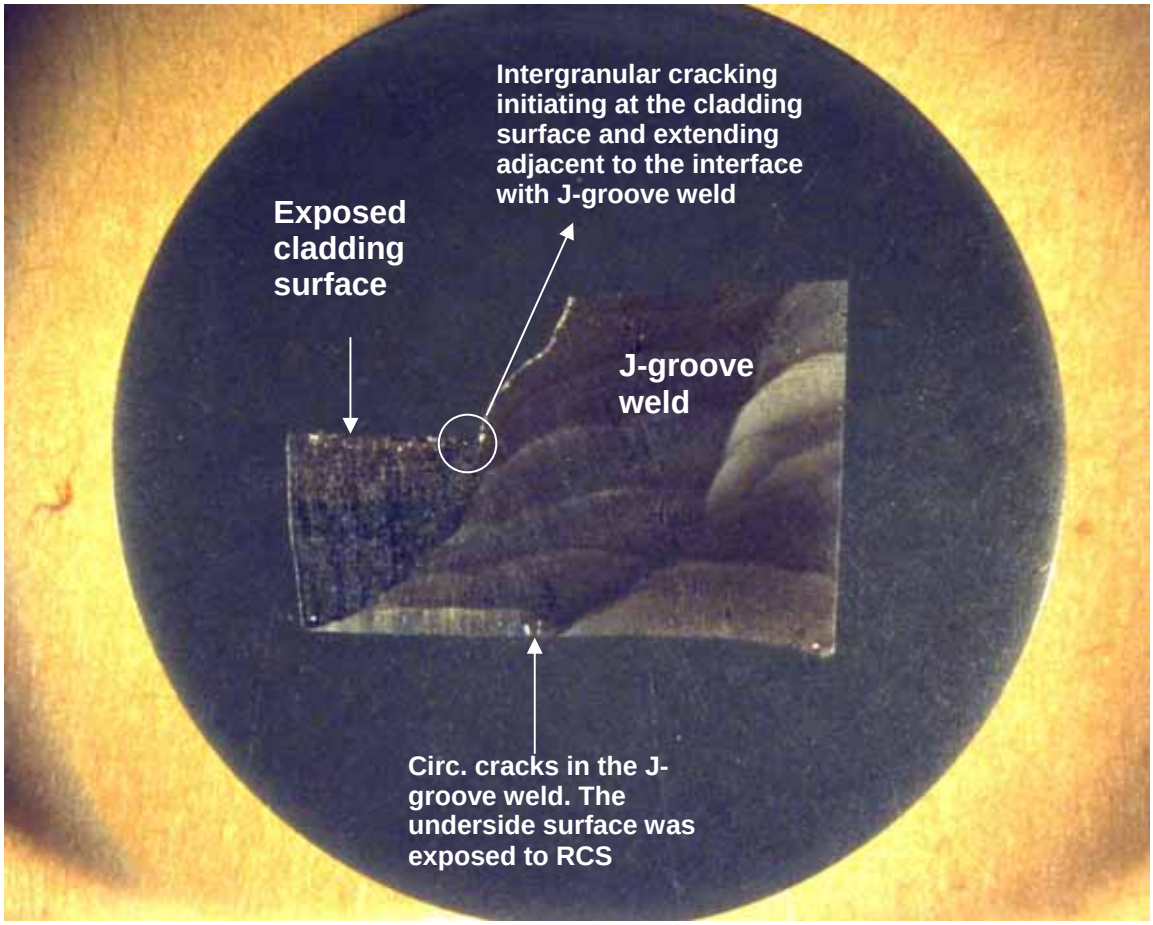

4X

Figure 7.3.2.1: Macro photograph of metallographic mount A2A6A2D2. The mounted surface is through the J-groove weld at ~30°. Refer to Figures 5.6 and 5.9 for the sample location.

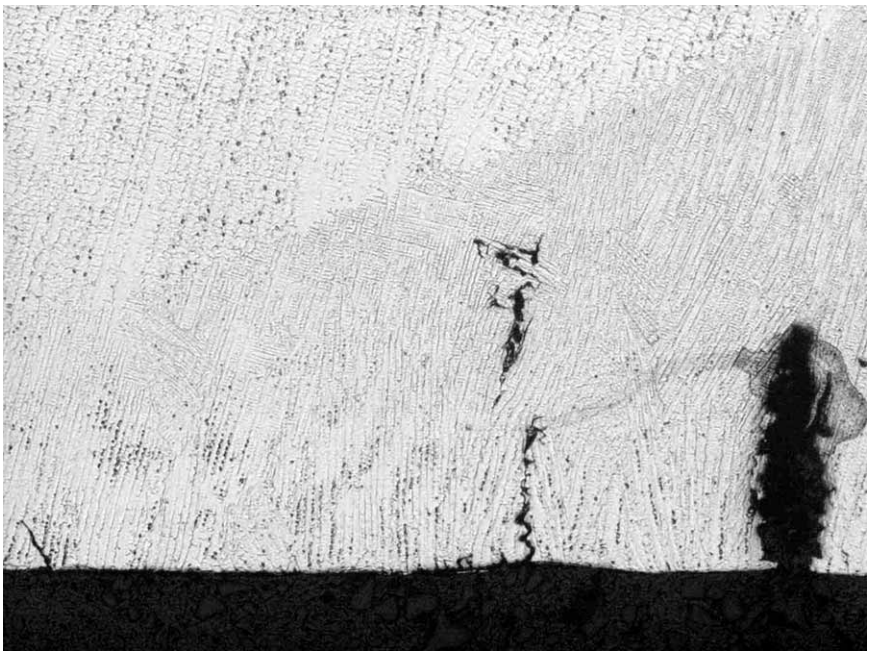

Etched 100X

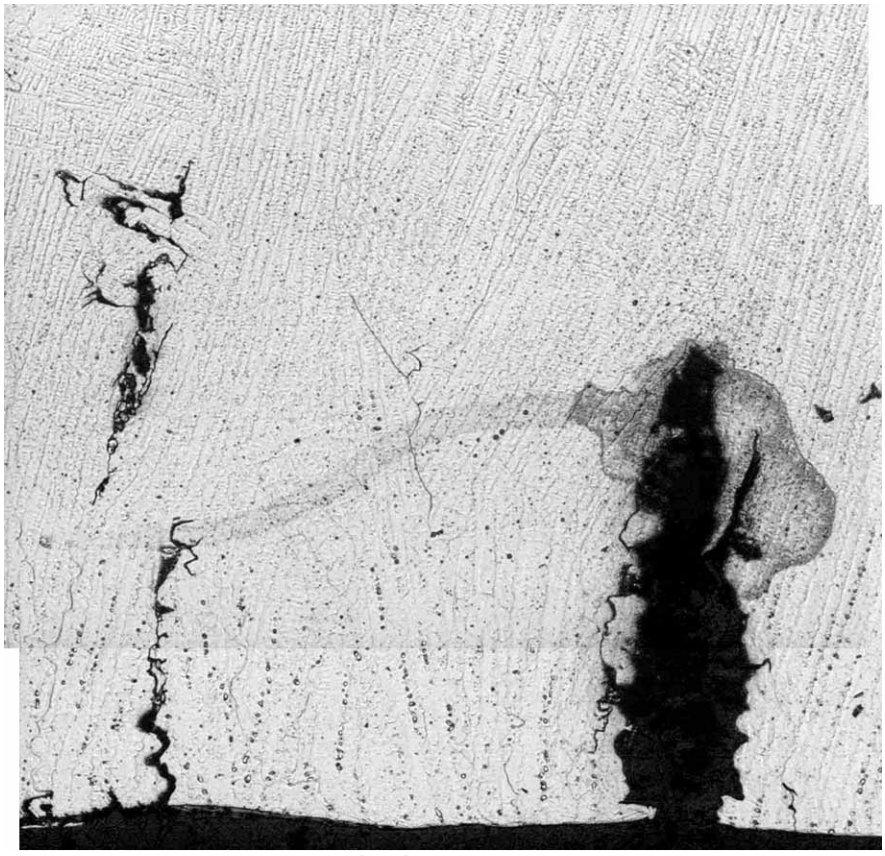

Etched 190X

Figure 7.3.2.2: Micrograph showing the circumferential intergranular/interdendritic cracks in the J-groove weld. The maximum cracking depth is approximately 0.018" below the surface. The cavity just below the surface may be due to dendrites or grains encircled by the cracks that dropped out during sample grinding and polishing.

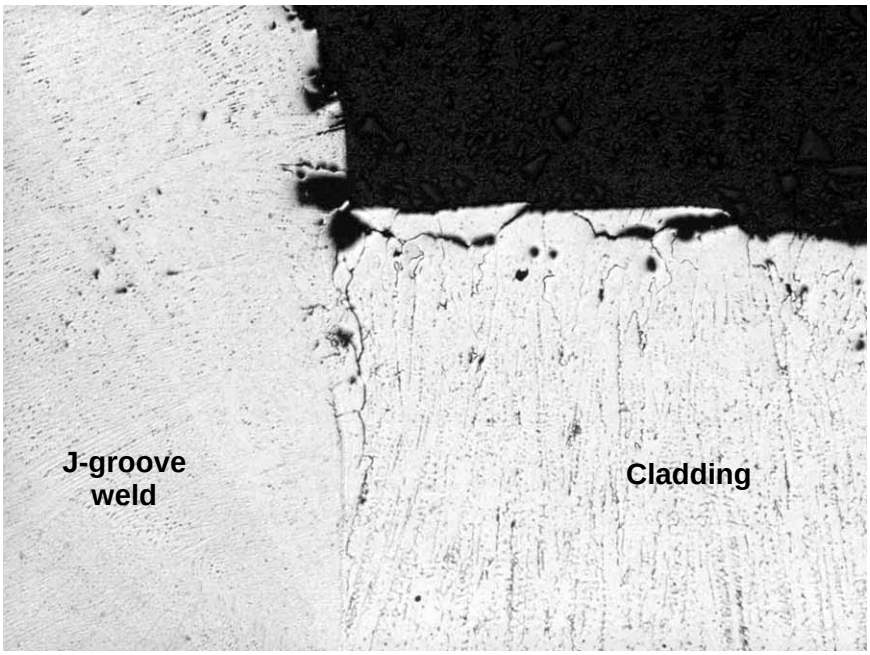

Etched 48X

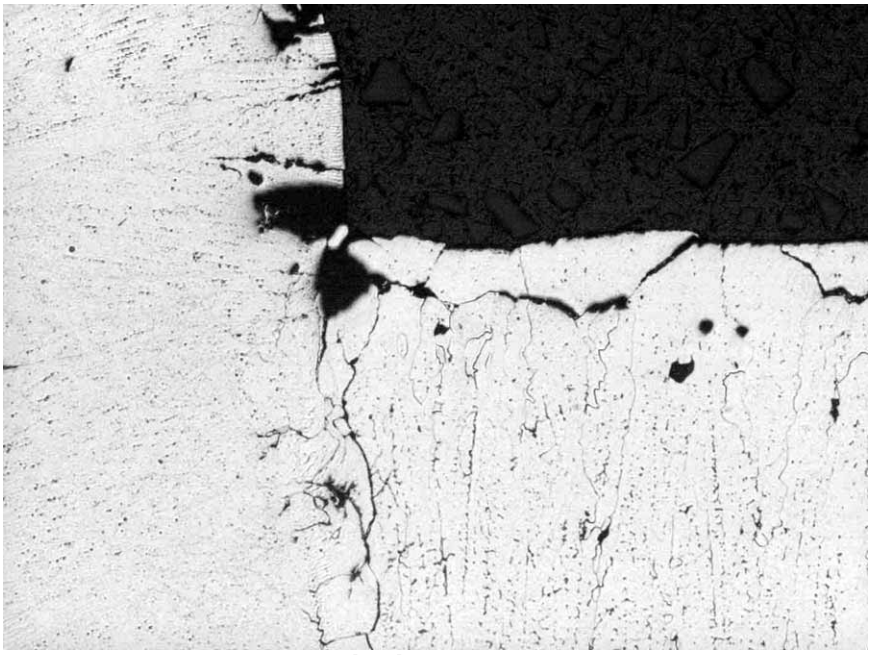

Etched 100X

Figure 7.3.2.3: Micrographs showing the intergranular or interdendritic cracking between the J-groove weld and cladding interface. The micrographs shown here are mirror of the photo in Figure 7.3.2.1. Intergranular attack (IGA) is also evident on the exposed surface of J-groove weld and cladding (surface exposed to oxygenated boric acid). This cracking was likely initiated by IGA.

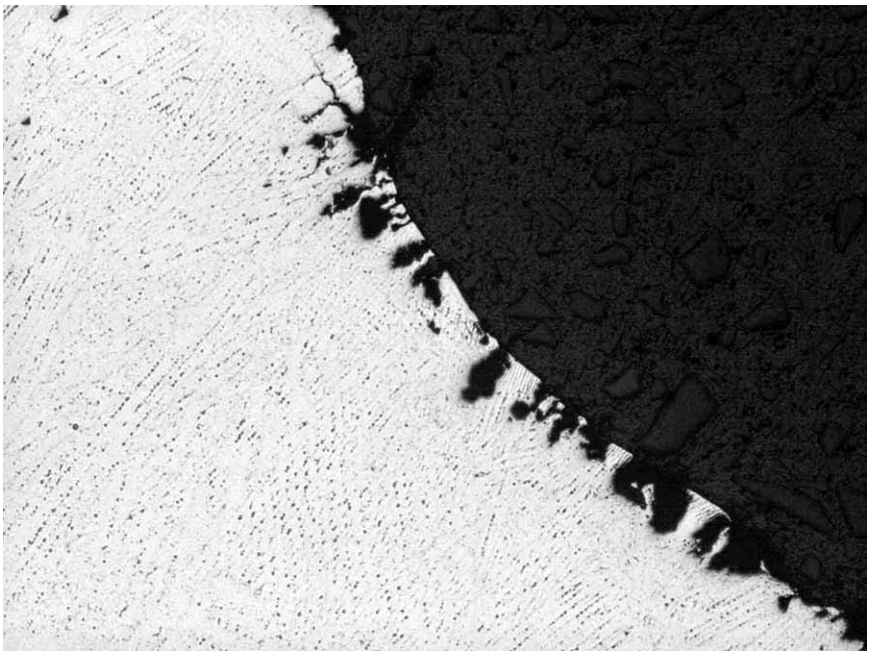

Etched 100X

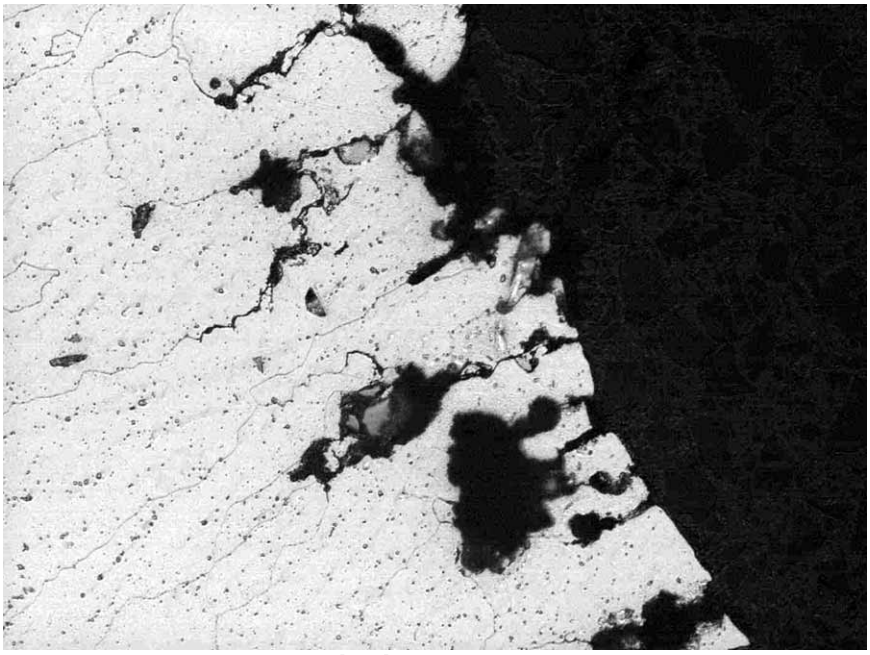

Etched 375X

Figure 7.3.2.4: Intergranular attack (IGA) on the J-groove weld surface exposed to oxygenated boric acid.

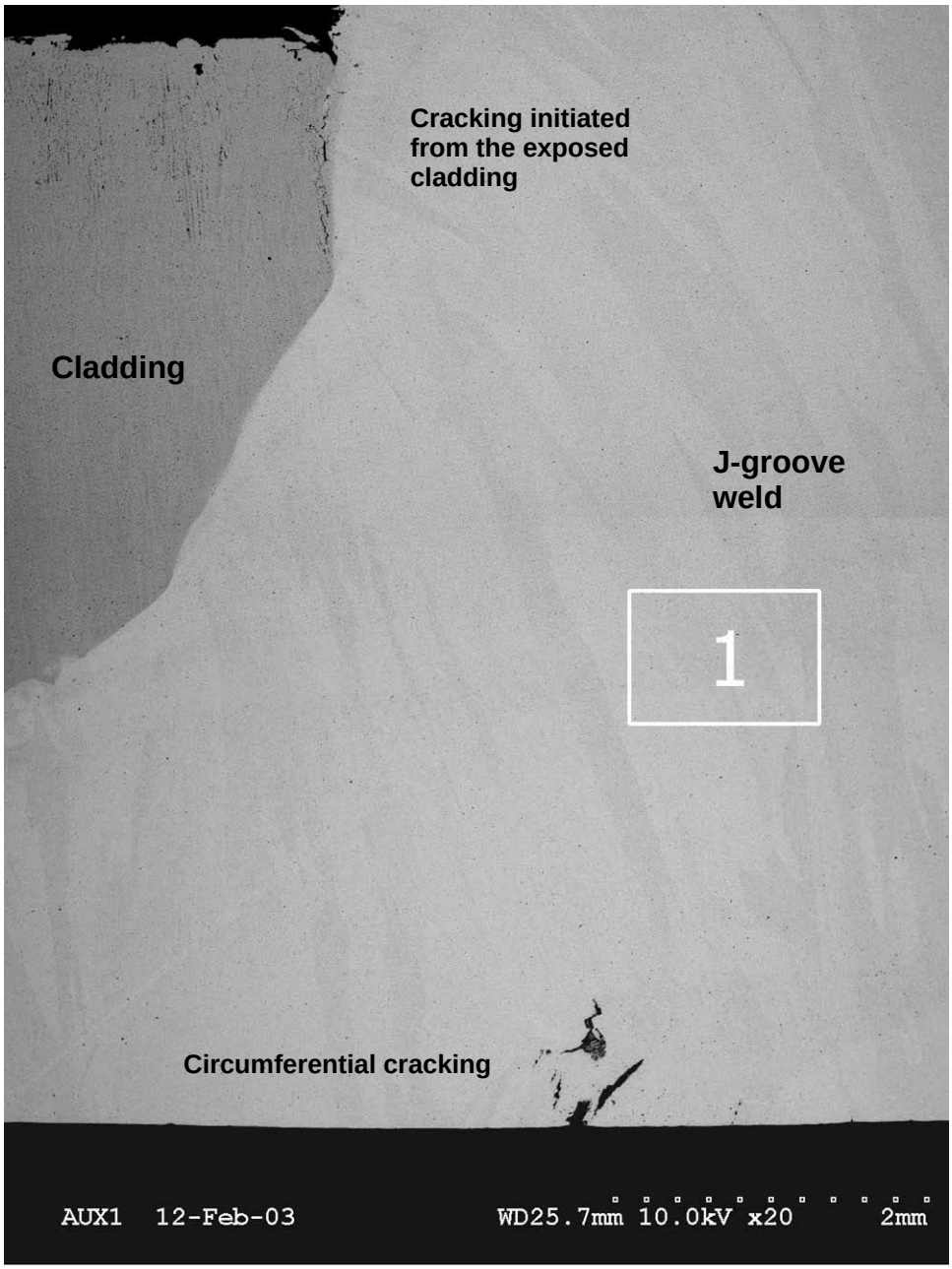

BSE 20X

Figure 7.3.3.1: Low magnification BSE micrograph of sample A2A6A2D2 showing the cracking in the exposed cladding surface and the axial cracking in the J-groove weld surface exposed to RCS. The EDS spectrum collected from area 1 is presented in Figure 7.3.3.2.

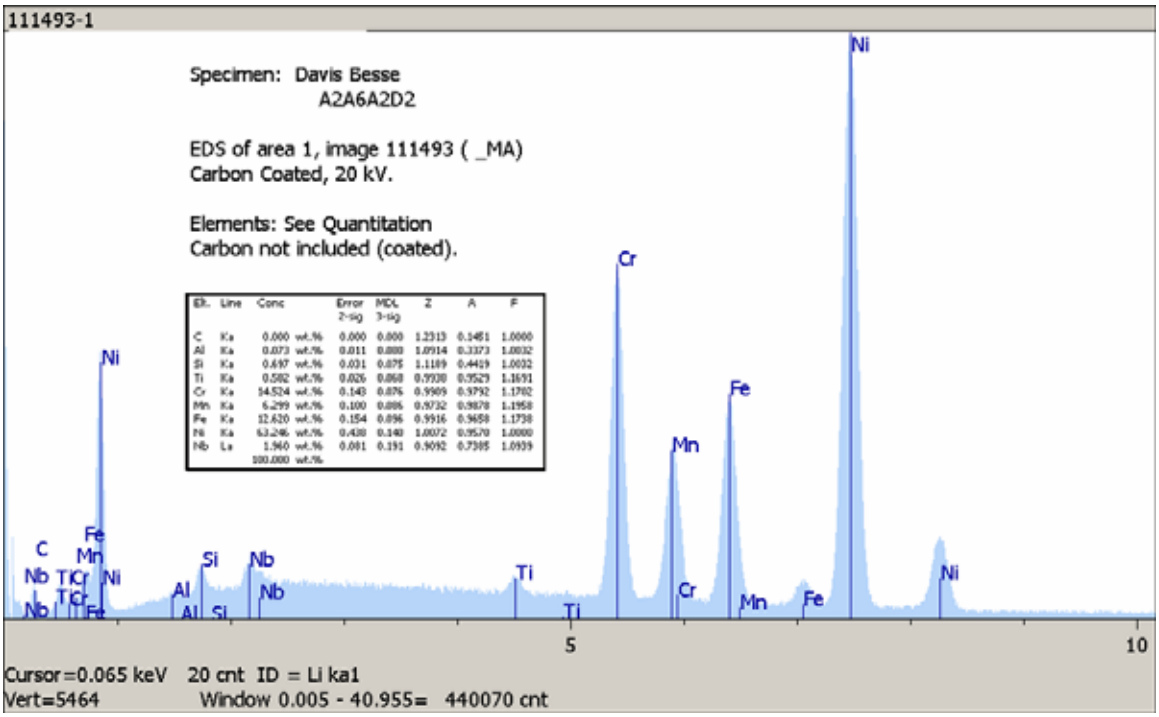

Figure 7.3.3.2: The EDS spectrum for area 1 in Figure 7.3.3.1. The semi-quantitative results from this area, which was located within the J-groove weld, were consistent with Alloy 182 weld metal.